ADVANCED OPTICAL MATERIALS
www.advopticalmat.de

Broadband Metamaterial Absorbers

Peng Yu, Lucas V. Besteiro, Yongjun Huang, Jiang Wu, Lan Fu, Hark H. Tan, Chennupati Jagadish, Gary P. Wiederrecht, Alexander O. Govorov, and Zhiming Wang**

The recent rise of metamaterials opens new opportunities for absorbers due to their designed electrodynamic properties and effects, allowing the creation of materials with effective values of permittivity and permeability that are not available in naturally occurring materials. Since their first experimental demonstration in 2008, recent literature has offered great advances in metamaterial perfect absorbers (MMPAs) operating at frequencies from radio to optical. Broadband absorbers are indispensable in thermophotovoltaics, photodetection, bolometry, and manipulation of mechanical resonances. Although it is easy to obtain MMPAs with single band or multiband, achieving broadband MMPA (BMMPA) remains a challenge due to the intrinsically narrow bandwidth of surface plasmon polaritons, localized surface plasmon resonances generated on metallic surfaces at nanoscale or high *Q*-factor in GHz region. To guide future development of BMMPA, recent progress is reviewed here: the methods to create broadband absorption and their potential applications. The four mainstream methods to achieve BMMPAs are introduced, including planar and vertical element arrangements, their welding with lumped elements and the use of plasmonic nanocomposites, accompanied by the description of other, less common approaches. Following this, applications of BMMPA in solar photovoltaics, photodetection, bolometry, and manipulation of mechanical resonances are reviewed. Finally, challenges and prospects are discussed.

1. Introduction

Artificially engineered materials, so-called metamaterials (MMs), demonstrate interesting electrodynamic properties, including negative refractive index,[1] electromagnetic (EM) wave cloaking,[2] and inverse Doppler effect[3] that are not found in naturally occurring materials. By engineering these composite structured materials, MMs can be viewed as homogeneous mediums with an effective permittivity and permeability.[4] As a particular subtype, MMs can be utilized as perfect absorbers, resulting in near unity absorbance over a small or a broad frequency band, while it can be crafted to overcome the thickness limitation of traditional quarter wavelength devices.[5,6] The thickness of a metamaterial perfect absorber (MMPA) can be about ≈25 times smaller than the resonance wavelength thickness of functional layers much smaller than their counterparts.[7] The MMPA, coupled with the strong growth of its applications, has provided motivation for further development. **Figure 1** summarizes some important publications in this field from 2008 to middle of 2017. Landy et al. first demonstrated a MMPA in the microwave regime utilizing a 2D MM electric ring resonator, in which electric and magnetic resonances match the impedance of free space, thus eliminating the reflection at the targeted wavelength.[5] This seminal work has sparked research to extend the MMPA concept to other frequency regimes and to a variety of applications.

Since the first demonstration of MMPA,[5] the advent of MMs has spawned extensive research into MMPAs over the last decade operating from radio to optical spectral range.[19–22] MMPAs have been demonstrated in applications, such as

P. Yu, Dr. L. V. Besteiro, Prof. J. Wu, Prof. A. O. Govorov, Prof. Z. Wang
Institute of Fundamental and Frontier Science
University of Electronic Science and Technology of China
Chengdu 610054, P. R. China
E-mail: govorov@ohio.edu; zhmwang@uestc.edu.cn
P. Yu, Prof. L. Fu, Prof. H. H. Tan, Prof. C. Jagadish
Department of Electronic Materials and Engineering
Research School of Physics and Engineering
The Australian National University
Canberra, ACT 0200, Australia
Dr. L. V. Besteiro
Institut National de la Recherche Scientifique – Énergie
Materiaux Télécommunications
Varennes, J3X 1S2, Québec, Canada
Dr. Y. Huang
School of Information and Communication Engineering
University of Electronic Science and Technology of China
Chengdu 611731, P. R. China
Dr. G. P. Wiederrecht
Center for Nanoscale Materials
Argonne National Laboratory
Lemont, IL 60439, USA
Prof. A. O. Govorov
Department of Physics and Astronomy
Ohio University
Athens, OH 45701, USA
The ORCID identification number(s) for the author(s) of this article can be found under https://doi.org/10.1002/adom.201800995.

DOI: 10.1002/adom.201800995

solar energy harvesting,[6,23,24] biological sensing,[10,25,26] thermophotovoltaics,[12,27] photodetection,[28–30] creation of imaging devices,[9,20,31] absorption filtering,[32] etc. For practical applications, the MMPAs can be divided into two types: narrowband and broadband. Although MMPAs with customized single-band,[5,33–35] dual-band,[22,36,37] triple-band,[38] and more[39,40] have demonstrated discrete absorption peaks, broadband absorbers attract much interest in both civilian and military applications, such as photovoltaics (PV), bolometry, photodetection, stealth technology, mechanical manipulation, etc. Unfortunately, achieving broadband absorption, especially in the THz region (and higher frequencies), still remains a challenging task because of the intrinsically narrow bandwidth of surface plasmon polaritons (SPPs) or localized surface plasmon resonances (LSPRs) generated on metallic surfaces at the nanoscale, which are exploited as a mechanism to obtain perfect absorption.[41] In GHz or lower frequencies, the resonant Q-factor, $Q = (1/R)\sqrt{L/C}$, is relatively large due to a lower effective resistance of the MMPA.[42] In order to increase the bandwidth of MMPAs, R is usually adjusted to yield a flatter, lower Q-factor.[42–45] Therefore, with a simple design, perfect absorption can be easily achieved at a single wavelength, but the design becomes complicated and difficult for absorbers with perfect absorption while achieving broadband absorption. Substantial progress has been made in developing broadband metamaterial perfect absorbers (BMMPAs), but the field remains immature. Previous reviews on metamaterial absorbers are mainly focused on absorbers in terms of their working frequencies ranges;[46,47] Watts et al. reviewed the theory behind perfect absorbers, along with details about their simulation and fabrication, and briefly discussed the applications of absorbers, including selective thermal emitters and spectrally sensitive detectors or sensors, but they did not put an emphasis on broadband metamaterials and their applications.[7] Zhao and Song reviewed BMMPAs fabricated by adding multiple resonators and dendritic structures in an unit cell.[48] In order to provide a guide for future development, this review comprehensively focuses on offering a comprehensive description of the state-of-the-art on BMMPA research, organizing these systems by their design approach. First, we review mainstream methods, by introducing BMMPA structures with planar and vertical resonators, lumped elements, and plasmonic nanocomposites and followed by some unconventional methods to fabricate BMMPA, such as using complementary metamaterial (CMM) structures, space-filling, dielectric tailoring, crossed trapezoidal resonators, and resonator material tailoring. Subsequently, we review some key applications of the BMMPA, such as PV energy harvesting, photodetection, bolometer, and manipulation of mechanical resonances. Finally, challenges and prospects of BMMPA will be discussed.

Peng Yu is currently a Ph.D. researcher in group of Prof. Zhiming Wang in the Institute of Fundamental and Frontier Sciences of University of Electronic Science and Technology of China. He obtained his bachelor's degree in Microelectronics in 2012 and master's degree in Electronic Information Materials and Components in 2015. His current research interests include metamaterial absorbers, quantum dot photovoltaic devices, and plasmonic applications.

Alexander O. Govorov is a distinguished professor of Theoretical Physics at Ohio University in Athens, USA. He received his Ph.D. in 1991 from the Institute of Semiconductor Physics in Novosibirsk, Russia. In 2001 he moved to the United States and joined Ohio University. His research focuses on the theory of optical and electronic properties of nanostructures, metamaterials, and bioassemblies.

Zhiming Wang is currently a professor in the Institute of Fundamental and Frontier Sciences of University of Electronic Science and Technology of China. He obtained his bachelor's degree in Applied Physics in 1992, master's degree in Semiconductor Physics in 1995, and his Ph.D. degree in Condensed Matter Physics in 1998. He did postdoctoral studies in Paul-Drude-Institute for Solid State Electronics, Berlin, Germany in 2000. His current research interests focus on epitaxial crystal growth, molecular beam epitaxy, quantum dots, surfaces, interfaces, nanostructures, nanoscience, and nanotechnology.

2. Typical Structure for BMMPA

MMPAs are usually composed of three layers: the periodically arranged metallic pattern, a dielectric spacer layer, and a continuous metallic plate. The first patterned layer is critical in MMPA design because it can be tuned to fulfil the impedance-matching condition with the environment, achieving zero reflection at resonant frequencies; the second dielectric layer is a spacer used to dissipate the EM wave; the metallic ground layer blocks all incident EM waves. The perfect absorption can be theoretically described using effective medium approximation,[49] equivalent circuit theory,[50] or interference theory[13,51]—these are comprehensively reviewed in refs. [7,46,52] The dominant mechanism of absorption is either dielectric loss in the second layer or Ohmic loss in the top pattern. In the case of Ohmic

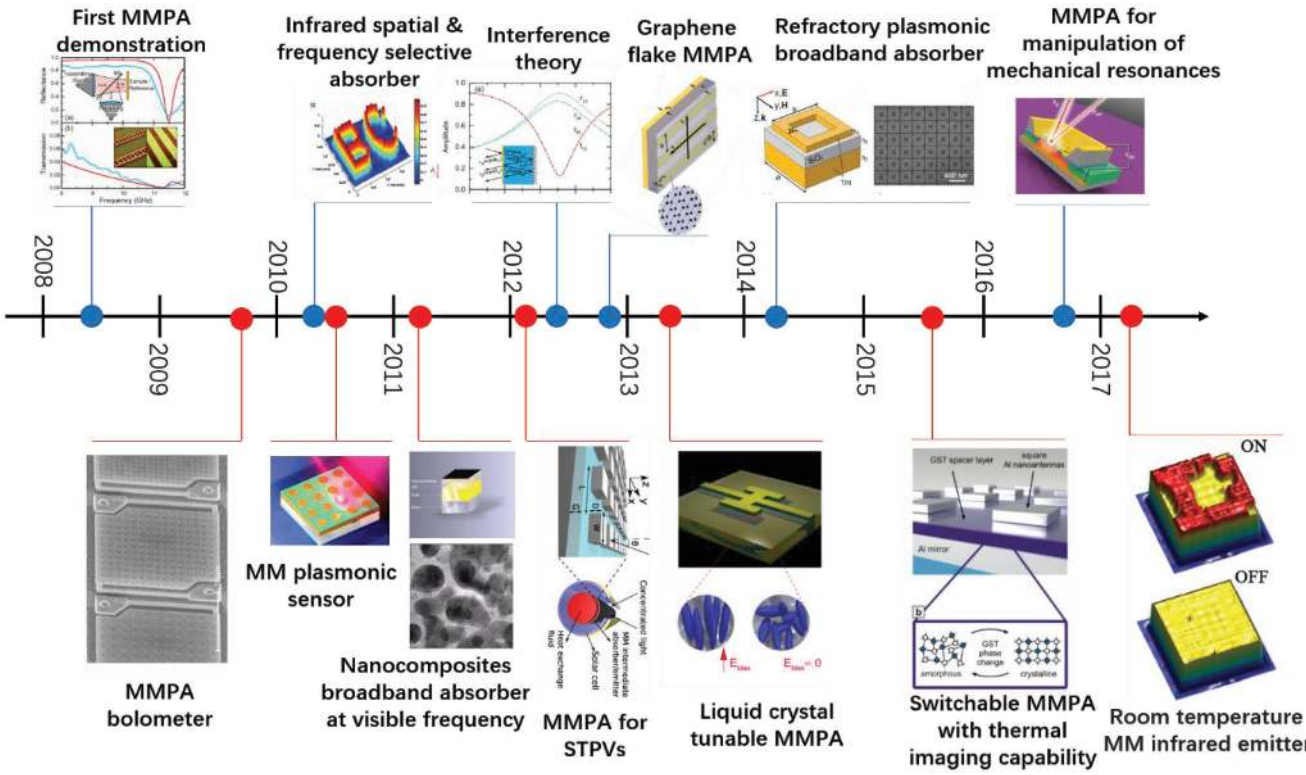

Figure 1. Selected representative publications on MMPA from 2008 to the middle of 2017. The publications highlighted here are cited as refs. [5,8–18], respectively, along the time axis.

loss, the *Q*-factor is reduced due to an increase of the bandwidth of the absorption peak, a key consideration for devising BMMPA.[46] A broadband response means that the device is able to absorb the entire EM frequencies that are illuminating the MMPA surface. In order to achieve panchromatic solar energy conversion, for instance, BMMPA is essential for light trapping in the solar cells.[53]

So far, researchers have experimentally and computationally demonstrated four main techniques to realize BMMPAs. One method creates multiple resonances in each unit cell via tailoring the size of the patterns on the top layer (planar arrangement), as shown in **Figure 2**a. Multiple resonances will appear and by incorporating resonators into a unit cell and perfect absorptivity can be achieved. Specifically, if these resonances are close enough, they will superpose with each other to form broadband absorption. It is worth noting that although the interaction from neighbouring cells has a shifting effect on the resonant frequency, the coupling strength is extremely weak.[54] The second method to yield a broadband absorption is to stack multiple top layers in the vertical direction (vertical arrangement), as demonstrated in Figure 2b. One can use different dielectrics and metals as an individual bilayer and finally stack these bilayers to form an unabated broadband absorption spectrum by tuning the geometrical parameters simultaneously. Figure 2c illustrates the third approach to design

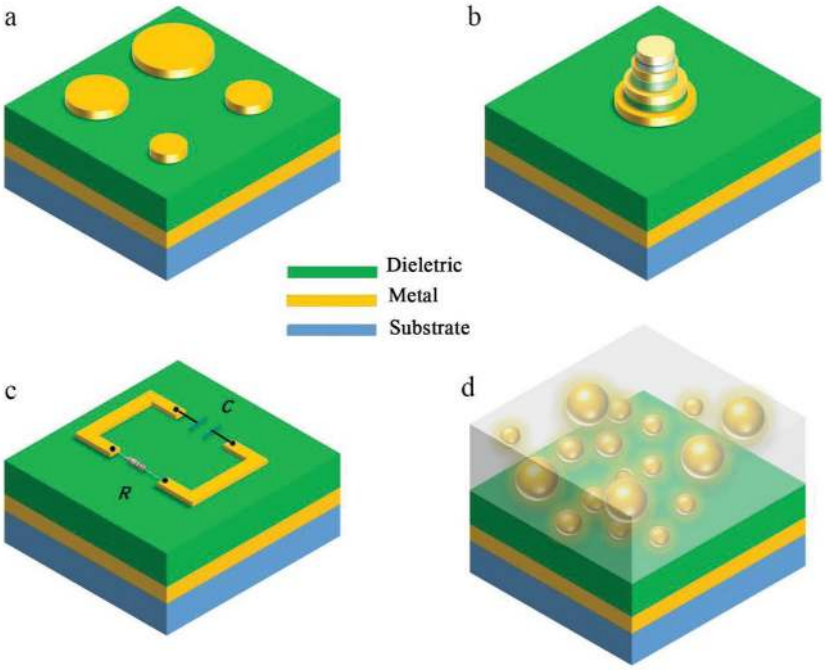

Figure 2. Conventional designs for BMMPAs. a) Planar arrangement, b) vertical arrangement, c) welded with lumped elements, and d) nanocomposites.

BMMPA: by introducing lumped elements such as resistances, capacitances, and diodes. The lumped elements—they are welded to connect the different resonant modes together and consume EM energy—reduce the *Q*-factor.[42] In the fourth method, the metal–dielectric nanocomposites take advantage of the LSPR from metallic nanoparticles (NPs), as illustrated in Figure 2d. The metal–dielectric nanocomposite systems provide impedance matching of the medium to free space, multireflection of light between the layers and light trapping and absorption by NPs, realizing perfect light absorption from UV to NIR.[11] In this section, we will describe four mainstream pathways to realize BMMPA, illustrated in Figure 2. Additionally, less common methods are also reviewed, including CMM structures, space-filling, dielectric material tailoring, crossed trapezoidal resonators, and the material tailoring of top resonators.

The prerequisite of BMMPA design is to provide multiple absorption bands. Therefore, it should be considered before realizing actual broadband absorption. Also, higher order harmonics of a single resonance structure,[37] extraordinary optical transmission,[55] CMM structure,[36] and Fabry-Perot-type cavity resonance in the dielectric[56] can be leveraged to achieve dual-band absorption and thus potential for BMMPA. Our previous work demonstrated that the snowflake-shaped MMPA shows multiband perfect absorption.[57] Therefore, recreating shapes found in nature with metals can also provide multiband perfect absorption, such as binary trees,[58,59] flowers,[60] and leaves.[61] Based on the following discussion, we compose **Table 1** to summarize the choice of metals and dielectrics in designing BMMPAs; only a few representative references are cited in the table.

Table 1. Metal and dielectric choice in BMMPA design.

Metal		Dielectric	
Ag	[24,26]	Ge	[40,82]
Au	[6,9,10,21,29,40,62,63]	Si	[30]
Cu	[38,64,65]	SiC	[83]
Al	[66]	ZnS	[40,84]
Mo	[36]	FR-4	[38,42,58,65,85,86]
W	[67]	SiN	[18,87]
Ti	[68]	GaAs	[40]
Pd	[69]	SiO_2	[11,36,62,64,88]
Cr	[70,71]	Al_2O_3	[6,9]
Ni	[72]	MgF_2	[10,29,77]
Ta	[72]	Water	[89]
ITO	[73]	TMM4	[90]
TiN	[16]	Kapton	[21]
AZO	[72]	Epoxy glass	[91]
Ta_2N_3	[74]	Polyimide	[63,66,92,93]
Graphene	[14,75–78]	Photoresist SU-8	[70]
Black phosphorus	[79]	Benzocyclobutane	[33]
Nanocomposite	[11,80]	Polydimethylsiloxane (PDMS)	[94]
$Ti_3C_2T_x$	[81]	Polytetrafluoroethylene (PTFE)	[11,80]
Conductive carbon black	[120]	Polyethylene glycol terephthalate (PET)	[73]
		Liquid crystal 4′-*n*-pentyl-4-cyanobiphenyl	[15]

2.1. BMMPA with Various Architectures

2.1.1. BMMPA with Planar Arrangements

Placing different metallic resonators with different sizes along the horizontal direction allows broadband perfect absorption due to the mixing of multiple resonances as long as $|\omega_0^{(i+1)} - \omega_0^i| < \Delta\omega_0^{(i)}$.[95] By designing resonators in a unit cell to be replicated throughout the *xy*-plane, it has a tangible effect on improving the bandwidth of MMPAs. Recent literature shows a great advance on BMMPAs operating at various frequencies. A BMMPA operating at mid-infrared using multiplexed cross resonators was theoretically and experimentally demonstrated,[62] as illustrated in **Figure 3**a–c. Compared with its counterparts with one and two resonators, the BMMPA with four resonators in a unit cell demonstrates absorption above 50%, preserved in a range of 1.86 (2.98–4.84) μm, while that of the one and two resonators are only 0.64 and 0.86 μm, respectively. The *Q*-factor drops as the number of crosses in a single unit cell increases. The square metal patch (SMP) is a commonly used structure in designing BMMPAs.[64,67] A BMMPA with four squares demonstrates greater than 90% absorptivity and near perfect impedance matching to the free space in the frequency ranges of 6.24–7.04 THz.[67] Almost simultaneously, another group proposed a BMMPA with absorptivity greater than 90% in the same frequency range of 6.24–7.04 THz.[64] They use different metals, showing the flexibility of BMMPA design. A THz BMMPA based on three I-shaped resonators demonstrated a broad and flat absorption over a wide range of incidence angle for either transverse electric (TE) or transverse magnetic (TM) polarization.[63] The overall absorption spectrum is ascribed to the superposition of individual components.

Circular metallic patches (disks) with different sizes in a unit cell are able to generate broadband absorption in the GHz region.[91] Lee et al. simulated cut wires with different lengths in a unit cell.[34] They concluded that the narrow peak in the GHz region was due to dielectric loss and the broad peak was due to Ohmic loss, elucidating two different mechanisms for energy dissipation. Conversely, rectangular hole arrays can be placed atop to obtain broadband absorption. A rectangular hole structure combined with a 90° anticlockwise rotation upon itself can excite mixed surface plasmons (SPs) at visible frequencies to support broadband absorption.[96]

Metal dendrites can also be used on BMMPAs because the structure is composed of branches with different length and size in the *xy*-plane, thus supporting multiple resonances.[58,59,73] Bao et al. first proposed a method by employing dendritic branch structures of different sizes to achieve broadband absorptivity from 9.79 to 11.72 GHz.[59] With densely arranged hexagonal metal dendritic units having different sizes, a BMMPA with isotropic absorptivity, larger than 50% in the S-band, ranging from 3.02 to 4 GHz, and greater than 80% in the X-band, ranging

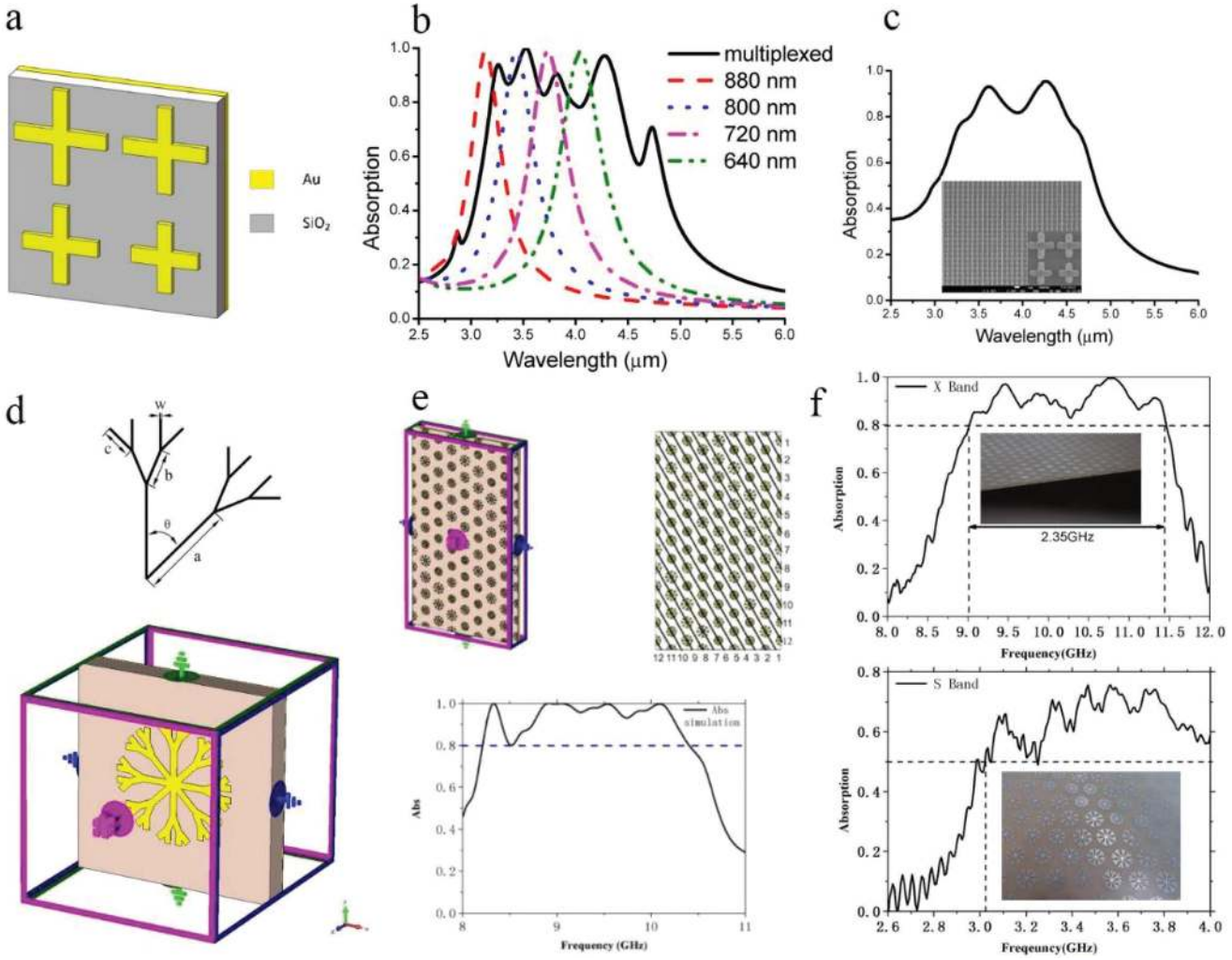

Figure 3. a) Unit cell schematic diagram of four cross resonators. The gold layer is 100 nm thick for the ground plane and 60 nm for the metallic patterns. The SiO_2 dielectric layer is 190 nm. b) Simulated absorption of multiplexed and four traditional non-multiplexed absorbers. c) Measured absorption for multiplexed absorber. The inset is a SEM image of the multiplexed absorber. d) Three-level dendritic structure and dendritic unit cell in the simulation model. e) The schematic of the X-band absorber composed of 12 kinds of independent units and its simulation result. f) The experimental results of the X-band and S-band absorbers. (a–c) Reproduced with permission.[62] Copyright 2013, Optical Society of America. (d–f) Reproduced with permission.[58] Copyright 2013, AIP Publishing.

from 9.05 to 11.4 GHz, has been demonstrated as shown in Figure 3d–f.[58] Recently, a BMMPA based on windmill-shaped resonators was reported to achieve broadband absorption, in an approach which was different from the common size variation route, as shown in **Figure 4**a.[73] In this structure, indium tin oxide (ITO) was introduced to be the top resonators' material, in order to tailor the Ohmic resistance of that layer. The Q-factor can be expressed as $Q = \omega_0 \times (P_T/P_L) = f_0/\Delta f$, where ω_0 and f_0 are the resonant frequencies. P_T and P_L are the stored and dissipated energy, respectively, while Δf is the absorption bandwidth. Increasing the resistance of ITO leads to a decrease of the P_L that lowers the Q-factor. When the surface resistance is 12 $\Omega\ \square^{-1}$ of the unit cell, the device achieves broadband absorptivity greater than 90% from 8.3 to 17.4 GHz, as shown in Figure 4b,c.

By modifying the size of the patterns and integrating them into a single unit cell, broadband absorption can be easily obtained. The combination of patterns with different shapes provides a route for achieving ultrabroadband spectral response. Abbott and co-workers demonstrated a retarder composed of an array of split-ring resonators and disk resonators working in the THz region.[94] Gu and co-workers propose a polarization-insensitive BMMPA absorber based on planar gradient structure MM, composed of resistor mounted crosswires and gradient split ring resonators (SRR) with a SMP in it, as shown in Figure 4d,e.[86] The presence of gradient resonators makes adjacent frequencies merge into a broadband frequency range. As a result, they observed that for both TE and TM waves, the operating frequency ranges from 12.38 to 22.28 GHz, where the absorption rate is above 60%, as plotted in Figure 4f. The enhanced absorption stems from the energy storage effect and difference resonances in the gradient structure. A "magnetic loop trap" structure is formed by the strong magnetic field generated around the SRR and SMP. The EM energy is confined

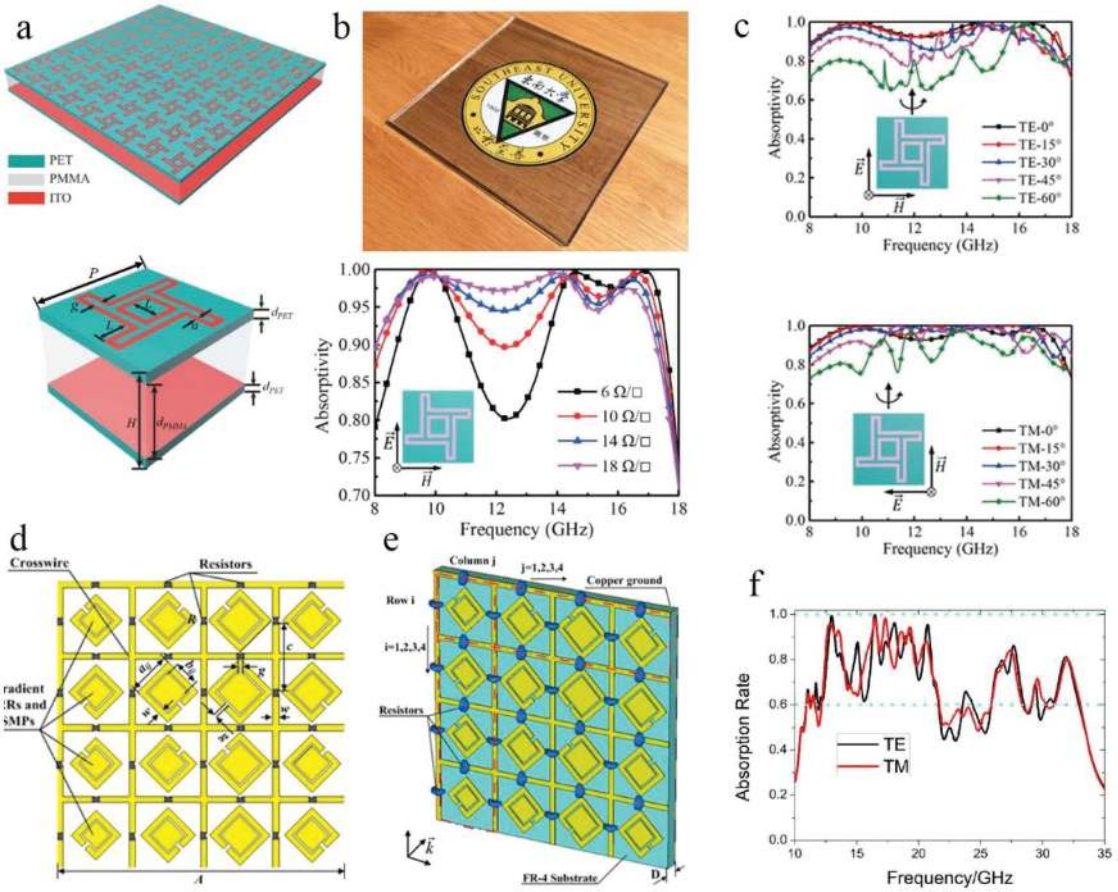

Figure 4. a) Schematics of an optically transparent BMMPA. b) Photograph of the fabricated sample and simulated absorptivity spectra with the increase of surface resistance of the ITO layer at normal incidence of TE wave, with the polarization direction illustrated in the inset. c) The angular dependence of the simulated absorptivity spectra for the MMA under the incidence of TE and TM waves, with the polarization direction and the incidence angle θ illustrated in the insets. The structure of the unit cell of a proposed integrated BMMPA: d) plan view and e) stereogram. f) The calculated absorption rate for both TE and TM wave. (a–c) Reproduced with permission.[73] Copyright 2017, AIP Publishing. (d–f) Reproduced with permission.[86] Copyright 2014, AIP Publishing.

within this structure, which effectively prevents the EM wave from leaking out. Therefore, current is excited on the top of the unit cell. By this means, EM waves could be consumed in the FR-4 dielectric substrates and the chip resistors.[86]

2D materials have attracted great attention due to their exotic optical transparency, flexibility, conductivity, and high electron mobility.[97] Low-loss graphene has an adjustable negative permittivity which enables spectral tuning of MMs, which can be used for amplitude tuning at the far-infrared and near-infrared frequencies. Graphene can be used on MMPA devices with tunability because the dielectric properties of graphene can be dynamically tailored by shifting the Fermi energy via chemical doping or electrostatic voltage.[14,75,76,98] For broadband absorption applications, Vasić and Gajić showed spectral tuning of MMPAs in the mid-infrared region.[76] Chaudhuri et al. demonstrated a BMMPA made of $Ti_3C_2T_x$ resonator exhibiting a high-efficiency absorption (≈90%) for a wide wavelength window (≈1.55 µm).[81] Zhang et al. proposed a tunable BMMPA based on graphene disks operating in the mid-infrared region.[75] They found that when the graphene's Fermi energy was 0.1 eV, the corresponding bandwidth with more than 80% absorptivity can be extended to 6.9 THz, with a full width at half maximum (FWHM) bandwidth of 10.1 THz. For frequencies that satisfy $\hbar\omega < 2E_f$, where E_f is the Fermi energy, the interband transition of graphene can be disabled while the intraband transition depending on the conductivity and spectral tuning will be dominant.

In this subsection, planar arrangements for broadband absorption of MMPA have been introduced. The structures discussed are capable of achieving broadband absorption at THz, GHz, and visible frequency ranges by placing resonators with different sizes and shapes on the *xy*-plane. Further work should emphasize the integration of more resonators in the THz and higher frequencies because the nanofabrication is becoming sophisticated. At the nanoscale, neighboring resonators in the *xy*-plane can influence each other and the number of resonators is limited within a period. Besides, future work should be focusing on investigating metal resonators with broadband absorption, for example, high loss metals. Graphene has attracted attention for its tunable permittivity from the visible to far-infrared region. Current work on graphene MMPAs has been limited to theoretical calculations, with no experimental

work yet reported due to the difficulties of atomic-level layer manipulation. Further work should be focused on validating the theoretical calculation and addressing the difficulties on atomic layer control of 2D materials, such as black phosphorus (BP), transition metal dichalcogenides (TMD), and graphene.

2.1.2. BMMPA with Vertical Arrangements

Although the planar strategy is an efficient method for broadening the spectral response while maintaining high absorption, the interval between two resonant frequencies might be too wide to merge due to the spatial constraint of introducing multiband design in the same layer.[39] Alternatively, placing resonators vertically can also extend the absorption spectrum. Zhang and co-workers stacked three dual-band subcells with different geometric parameters to form a BMMPA.[99] An annular pattern is on the top surface and a metallic circular patch is located at the bottom of each subcell. As a result, the BMMPA shows a continuous absorption spectrum between 8.8 and 10.8 GHz with absorptivity all above 80%. The FWHM absorption bandwidth is 2.3 GHz (8.7–11 GHz). Although the square lattice is usually created for narrow band absorption, in this case it was stacked to form a BBMPA with a truncated pyramid structure, working in the full infrared region.[70,100]

Slowlight waveguide modes of weakly coupled resonances in various patterns are proposed for broadband absorption.[90,101] The stacked anisotropic MMPA allows the excitation of slow-wave modes in tapered, alternating metal–dielectric thin films, used to "stop light."[82,102] Light of a specific wavelength is slowly "squeezed," which is slightly different from the abovementioned vertical stacking—while they yield a broadband absorption by superposing a series of narrow absorption peaks, the slow light effect does not use direct superposition because the layers are too thin to support localized resonances. The incident energy propagates through the z-direction without penetrating into the resonators and then whirls into the resonator region. Vortices are formed close to the interface between the resonator and air regions with concentrated EM field. Quadrangular pyramidal frustums composed of 20 stacked metal patches, with their width tapered linearly from bottom to top were demonstrated by He and co-workers, as shown in **Figure 5**a–c.[102] The device's experimental versus simulation absorptions are compared in Figure 5d. It achieves nearly unity absorption from 8 to 14 GHz over a wide angular range and the measured relative bandwidth is 61.6% while the simulated is 53.1%. The broadband response can be easily understood by examining the electrical and magnetic distribution. At short wavelengths, EM absorption is primarily located at the tapered top, while for longer wavelengths the EM absorption is primarily located at the bottom. Additionally, the absorption is nearly independent of the incidence angle below 40°. At the same time, the slow-light waveguide can be obtained by etching a metal slab into a sawtooth shape with the tooth widths increasing gradually from top to bottom, as demonstrated in Figure 5e.[82] As a result, the absorptivity is higher than 95% and preserved for a wide frequency range due to gradual change of effective indexes, as shown in Figure 5f. Meanwhile, the BMMPA maintains high and ultrabroadband absorption when the incident angle is smaller than 60°. Figure 5g shows that the fundamental propagating mode has an extreme point with low group velocity, that is, $|v_g|/c$ approaching 0, mirroring slow light modes present in the simulated structure. With $v_g = 0$ for different values of W and teeth widths at the central energy allows waveguides with W from 150 to 600 nm to support slow light modes.

Xiong et al. proposed a stacked BMMPA structure utilizing destructive interference mechanisms.[90] It maintains a 90% absorption band spanning from 8.37 to 21 GHz with a thickness of 0.10–0.26 free space wavelength. Being different from the gradually size-changing resonator at the vertical direction, there are some examples in the literature demonstrating BMMPAs by embedding patterns in the dielectric spacer with different distances.[93,103] For example, a three-layered cross resonator embedded in polyimide shows three resonances at 4.32, 5.31, and 5.71 THz, as the schematic shown in **Figure 6**a.[93] Since the three peaks are close enough, they form a wide frequency band from 40.8 to 5.94 THz, where the absorption is greater than 60%, as shown in Figure 6b; the FWHM of the absorption is 48% of the central frequency of the three-layer structure.

Graphene can be vertically stacked.[77,78,104–106] Chen and He simulated a graphene-based BMMPA which consists of an array of graphene–dielectric multilayered pyramidal frustums with a homogeneous metal film, as shown in Figure 6c.[78] Since the shape of the resonator is unchanged, the pyramidal shape is then tapered linearly from bottom to top, to breed different resonances with a subtle progression. The spectrum in Figure 6d indicates the performance is excellent, with absorption around 90% covering the frequency range from 10 to 22 THz. The localized EM wave gives an intuitive interpretation for broadening: as the frequency increases, it moves up gradually toward the top of the pyramid structure. Moreover, they found that both the slow wave mode and Floquet periodic mode contributed to absorption. To expand the near-unity bandwidth absorption in the THz region, Amin et al. first adopted an asymmetric graphene pattern to excite quadrupolar SPPs, in comparison with graphene absorbers designed to operate only in their dipolar mode, as shown in **Figure 7**a.[105] The absorption of three-layer stacking design in Figure 7b demonstrates a band of 90% absorption from 4.7 to 11.6 THz. By repeatedly stacking graphene/MgF_2 layers, another group achieved a broad absorption band in the THz region as well.[77] Afterward, a BMMPA with two left-handed and two right-handed helices of graphene has been proposed to achieve perfect absorption covering from ultraviolet to near-infrared, that is, 200–1792 nm.[104] By utilizing many-particle effects, a nano-cross-elliptical hole structure embedded in multilayer graphene stack was proposed to enhance the absorption of graphene and extend the bandwidth.[106]

Compared with graphene and TMDs, BP has a remarkable direct bandgap (≈0.3 eV) in bulk, while the 2D BP provides a thickness-dependent direct bandgap ranging up to ≈2 eV for monolayer BP. An IR absorber, based on 2D BP MMs sandwiched between dielectric layers, was proposed to achieve extremely broadband absorption ranging from ≈30 to 80 μm,[79] with its design shown in Figure 7c. Interference theory was introduced to reveal the mechanism behind the observed absorption phenomena, as shown in Figure 7d. The destructive

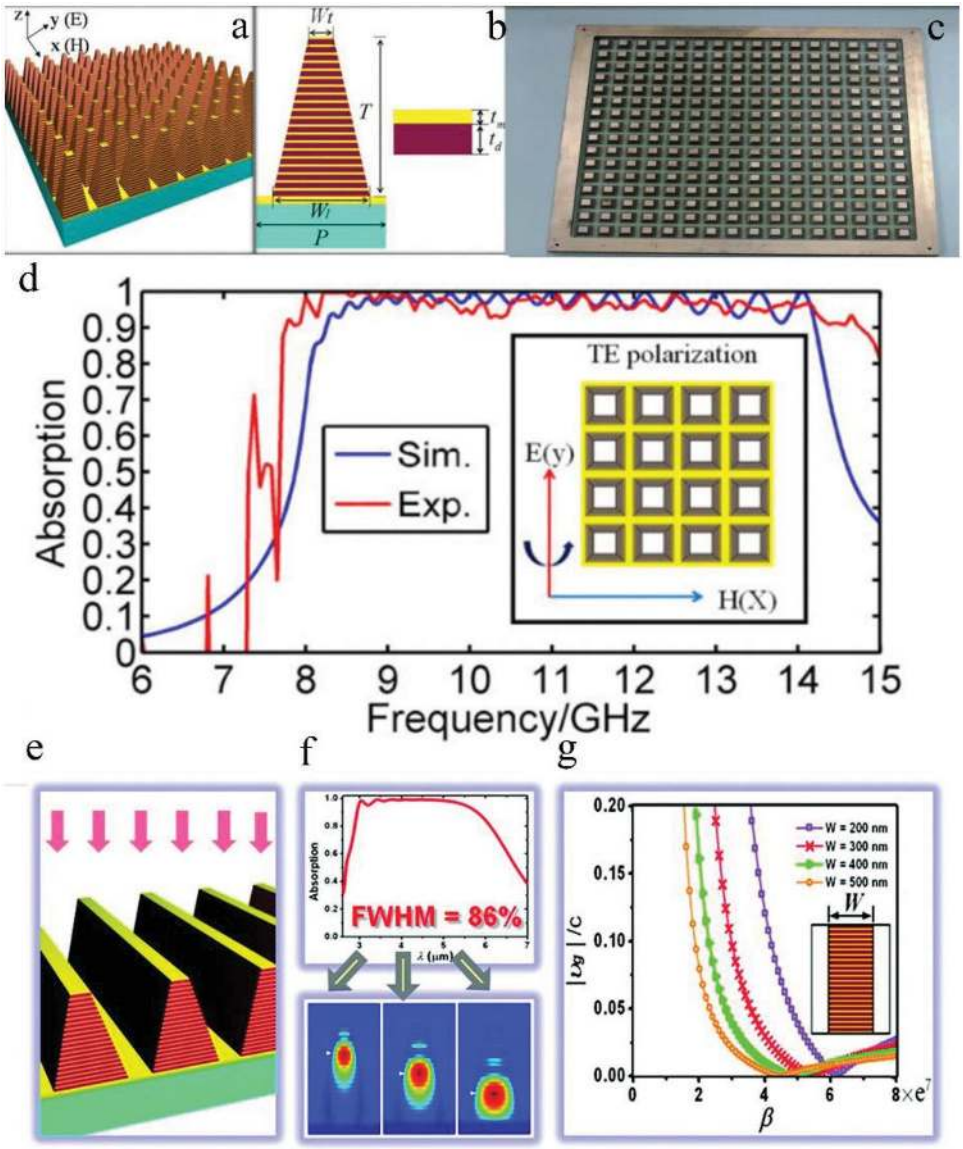

Figure 5. a) 3D illustration of the simulated MMPA, b) schematic of a MMPA unit cell, and c) photograph of the fabricated sample. The optimized dimensions of a unit are W_t = 5 mm, W_l = 9 mm, P = 11 mm, t_m = 0.05 mm, t_d = 0.2 mm, and T = 5 mm. Subscript "m" represents copper, and "d" for FR4. d) Comparison between the simulated absorption (blue line) and experimental absorption (red line). The inset shows the configuration of the incident wave. e) Diagram of the sawtooth anisotropic MM thin film absorber. Light of TM polarization is incident along z-direction. f) Absorption spectra for the sawtooth MMPA and distributions of magnetic field corresponding to 3.5, 4.5, and 5.5 μm, respectively. g) Relationship between the group velocity and propagation constant (proportional to wavevector) at different W. (a–d) Reproduced with permission.[102] Copyright 2012, AIP Publishing. (e–g) Reproduced with permission.[82] Copyright 2012, American Chemical Society.

interference between the directly reflected wave and the following multiple emergent waves effectively captures the behavior of the BMMPA, giving rise to the high absorption. The electric field intensity at the z-direction in Figure 7e is shown for TM polarization with λ = 54.3 μm, where the number of layers in the sandwich-like structure (NLSS) decreases from 4 to 1. The field enhancement is primarily concentrated around the edge of the BP nanoribbon and the absorption increases with increasing NLSS. The distance D between neighboring BP nanoribbons and their thickness affect the absorption performance, as shown in Figure 7f. For $D \neq 0$, absorption rates greater than 90% are achieved if D is less than 80 nm, while for D = 0 nm the absorber performance is evidently reduced. The attenuation can be ascribed to the fact that the MM structure no longer exist after merger. By changing thickness Δ, and thus changing the bandgap, the absorption peak position exhibits a blueshift with decreasing Δ. The proposed absorber achieves a perfect absorption for bilayer and trilayer BP MMs when nanoribbon width w = 230 nm.

In this subsection, we have reviewed BMMPAs with vertical arrangements. The BMMPAs with vertical stacking are relatively more effective for broadband absorption than their

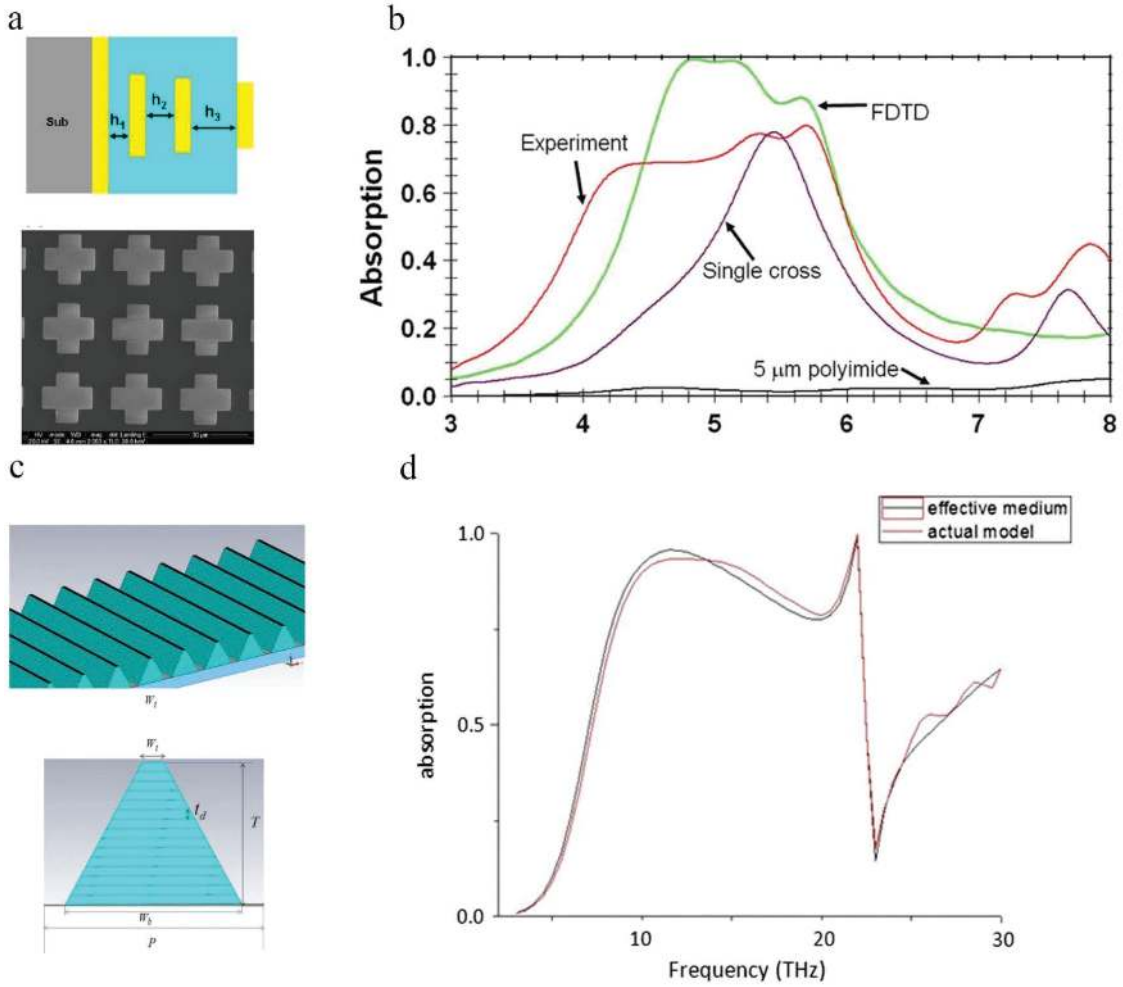

Figure 6. a) Cross-section illustration and SEM image of the complete multilayer absorber. b) Experimental and simulated data of the multilayer absorber. Also plotted is the experimental absorption spectrum for a single-layer absorber. c) Schematic diagram for a line array of graphene-dielectric multilayered quadrangular pyramidal frustums backed with a homogeneous metal film. A unit cell of the graphene BMMPA is illustrated, with $P = 10$ μm, $w_b = 8$ μm, $w_t = 1$ μm, $t_d = 400$ nm, and $T = 6$ μm. Light with TM polarization is incident along z-direction. d) Absorption spectra for a graphene-dielectric multilayered pyramid absorber with $N = 15$ periods and thickness of dielectric layers equal to 400 nm. The red line is the result of the real structure, and the effective homogeneous mode is shown by the black line. (a,b) Reproduced with permission.[93] Copyright 2011, Optical Society of America. (c,d) Reproduced with permission.[78] Copyright 2013, IEEE.

planar counterparts, but they are typically bulkier because of the stacked layers. Fabricating multiple aligned patterns is complex and time-consuming. 2D materials are attractive for designing THz absorbers, especially for vertical stacking in BMMPA designs, for the following reasons: 2D layers can support SPPs at THz frequencies; the atomic-scale stacking circumvents the trade-off between stacking thickness and absorption; frequencies tunability can be achieved by biasing the layer. However, due to its atomic thickness, a single layer of 2D material remains practically transparent to THz waves and, as a result, the overall absorption is significantly reduced. To enhance the absorption of 2D materials, different means have been investigated, such as using graphene-based gratings,[107] exploiting the quantum dots near graphene[108] and plasmonic effect.[106] Moreover, methods permitting a facile operation in controlling the layers of 2D material and their doping still need improvement.

2.2. BMMPA with Lumped Elements

Following equivalent circuit theory, metallic patterns can be understood as equivalent inductors and capacitors to approximately determine their resonant frequencies.[50] Then, lumped resistors are introduced to connect the gaps of resonant patterns. Compared with traditional MMPAs with only metal structures and dielectric substrates, MMPAs loaded with lumped elements (resistor, inductor, capacitor, and diode) provide advantages such as tunability and spectra broadening.[42–45,109–111] The lumped elements are loaded by welding to connect the different resonant modes together and consume EM energy. Typically, the Q-factor in electrically coupled LC (ELC) and SRR MMPA is defined by $Q = \sqrt{LC}/R$, where L and C are the inductance and capacitance of the equivalent inductor–capacitor circuit. Increasing the resistance R yields a flatter, lower Q-factor, while decreasing R leads to a sharper, higher Q-factor. To further

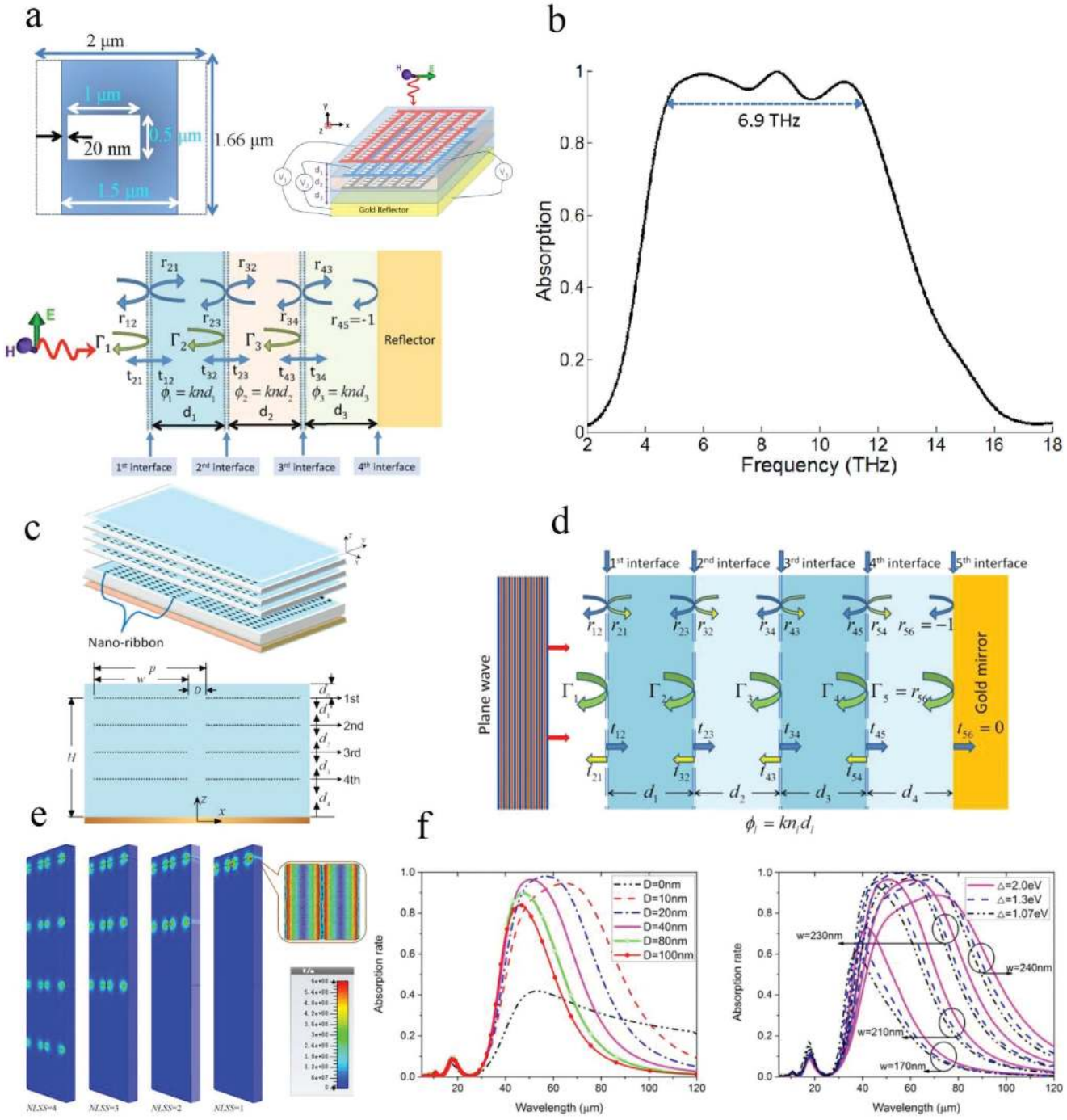

Figure 7. a) The schematic diagram of the proposed absorber with three layers of graphene (top right). The graphene unit cell with an asymmetric void with its dimensions (top left). Description of the transmission line model for the multilayered absorber (bottom). b) The absorption spectra of the three-layer design with $d_1 = 0.67$ μm, $d_2 = 0.5$ μm, and $d_3 = 4.78$ μm. c) Schematic of the proposed sandwich-like structured BP absorber and front view of the proposed absorber with layer dimensions. d) A schematic diagram of the transmission and reflection for a four-layered sandwich-like BP structure. e) Simulated average electric field intensity values for monolayer BP MMs with two nanoribbon periods aligned along the *x*-direction. The inset presents a sectional view at the in-plane across the first interface for NLSS value of 1. f) Simulated absorption rate spectra for TM polarization at various distances between two nanoribbons and for various thicknesses of BP in monolayer, bilayer, and trilayer with ridges perpendicular to the *x*-direction. (a,b) Reproduced with permission.[105] Copyright 2013, Optical Society of America. (c–f) Reproduced with permission.[79] Copyright 2017, Optical Society of America.

decrease the *Q*-factor, the elements are embedded into the MM structure.[42] A split-coin resonator BMMPA welded with lumped resistances demonstrates an absorptivity of 90%, with 1.5 GHz bandwidth and a FWHM of up to 50%, as shown in **Figure 8**a,b.[45] The geometrical parameters of the system are defined in Figure 8a, noting that it is not limited by the quarter

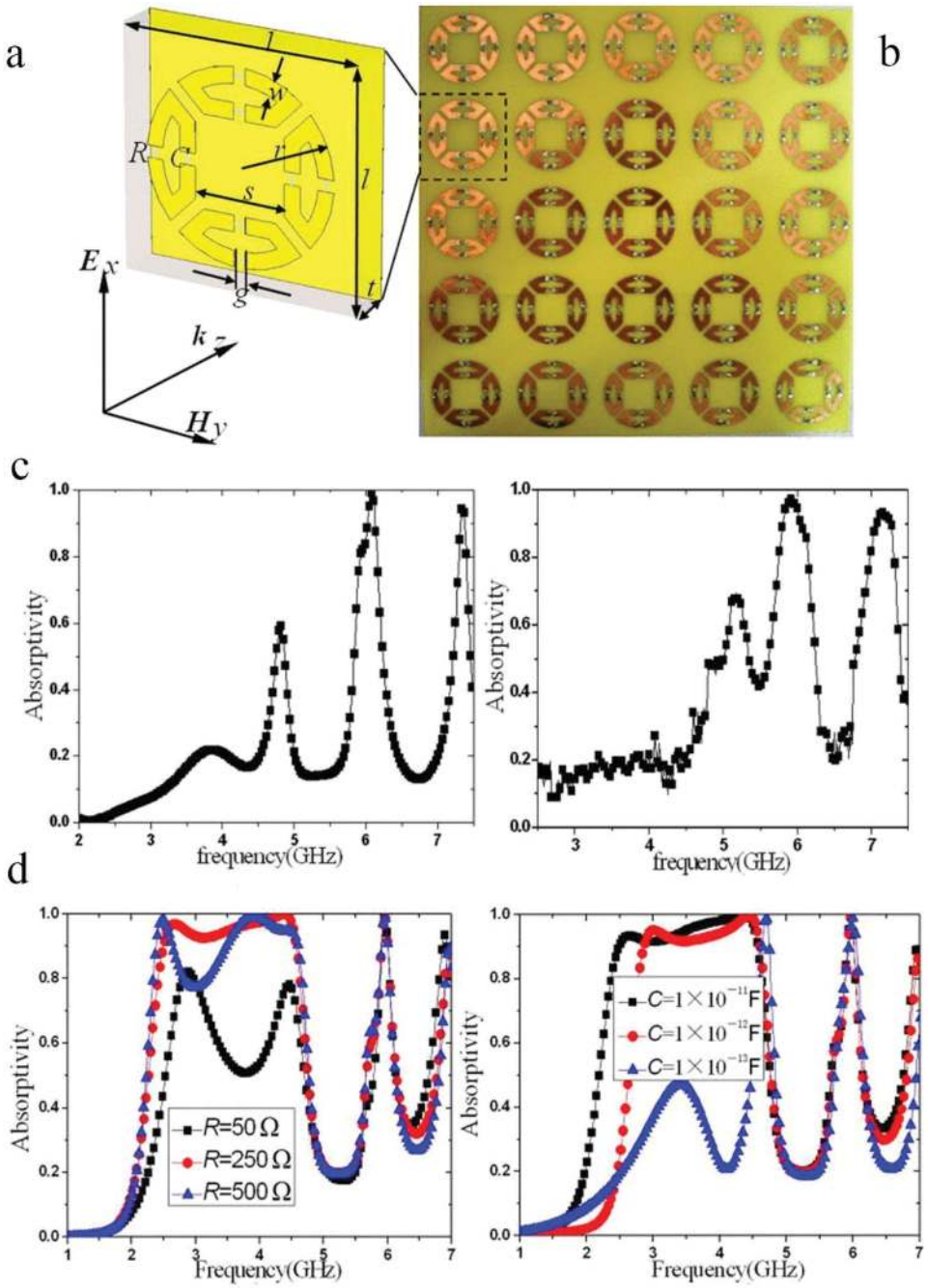

Figure 8. a) Perspective view of unit cell with indicated TEM wave direction and geometric dimensions and lumped parameters: l = 40 mm, r = 16 mm, s = 15.2 mm, w = 2.7 mm, g = 2 mm, t = 6 mm, C = 4 pF, R = 249 Ω. b) Photograph of fabricated lumped elements BMMPA sample. c) Absorptivity of MMPA before introducing lumped elements: absorptivity of the simulation (left) and experimental results (right). d) Absorptivity of the BMMPA with different values for the lumped elements: lumped resistance R (left) and lumped capacitance C (right). Reproduced with permission.[45] Copyright 2012, AIP Publishing.

wavelength thickness and it is relatively thin (≈λ/10) in the propagation direction. Before loading the lumped resistors the absorption is narrow, with two peaks at 5.9 and 7.2 GHz, as shown in Figure 8c. However, after introducing the lumped resistances, the simulated absorptivity exceeds 90% from 3.1 to 5.6 GHz and the FWHM is up to 55% while maintaining high absorption, as shown in Figure 8d. When C = 4 pF and R = 250 Ω, the absorptivity peaks and the bandwidth extends from 2.2 to 4.7 GHz, with the FWHM increasing to 72%. However, when C = 10 pF, the performance of BMMPA is the best due to reduced Q-factor. While the lumped resistance mainly influences the magnitude of absorptivity, the lumped capacitance influences both the magnitude and bandwidth of absorptivity, as observed in Figure 8d.

Double rings loaded with lumped resistances have been validated in their broadband absorption properties.[44,109] A double-circle ring BMMPA yields a 7.60 GHz wide absorption from 8.87 to 16.47 GHz with absorptivity greater than 90%.[44] A thin and polarization-insensitive BMMPA, created by loading eight lumped resistors into double octagonal rings, has been investigated by experimental and computational methods.[109] The results achieved a 9.25 GHz wide absorption from 7.93 to 17.18 GHz, with absorptivity larger than 90% at small incident angles, from 0° to 20°. The electrical field distributions of this structure indicate that high absorption can be ascribed to the rings and resistances in the system. Periodic arrays of metallic strips are connected to achieve thin and polarization-insensitive BMMPA.[110] The thickness of the absorber is 3 mm, which is almost 1/17 of the free space wavelength at the lowest frequency of 6 GHz. In addition to connecting the resonators via resistors and capacitors, chip resistors and PIN diodes were also used to provide both a broadband absorption profile and switching capabilities.[112] The absorber switched between two frequency bands from 8.45 to 9.3 GHz and 9.2 to10.45 GHz, when the PIN diode is switched to ON and OFF states, respectively. A BMMPA with four lumped resistors loaded in the gap between each fan-shaped circular sector achieved absorptivity over than 96% in the frequency range of 7–12.8 GHz.[113]

Lumped elements are welded between the resonators to reduce the *Q*-factor of MMPAs and thus achieve broadband absorption. However, this method is limited to the GHz spectrum, where radar applications operate. With nanoscale resonator fabrication processes, introducing equivalent lumped elements is a tough task. One can transfer this method to THz or infrared frequencies, however, connecting the resonators equivalent with the lumped elements needs accurate alignment during fabrication process.

2.3. BMMPA with Plasmonic Nanocomposites

In a typical MMPA structure, the contribution of metallic absorption is dominant when the device is operating at NIR or in the visible spectrum. Therefore, the role of dielectric absorption is less important at these frequencies and the device can be made thinner for high-frequency application. Metallic NPs offer tailored plasmonic response for absorption and scattering enhancement at their resonant frequency.[114,115] The top layer is substituted by an ultrathin (≈20 nm) plasmonic nanocomposite made of metal NPs dispersed randomly in polymeric (or generally dielectric) matrix. By combining impedance matching of the medium to free space to avoid reflection at the outer layer, multiple reflection of light between the layers and light trapping and absorption from the tiny metallic particles, the nanocomposite BMMPAs have been shown to operate in a wide spectral range from UV[11,116] to visible[80,117,118] and NIR.[11,118,119]

A high density nanocomposite can lead to broadband absorption due to excitation of localized plasmon resonances of the NPs by visible light.[119] Gold,[11] copper,[80] and silver[116,119] nanocomposites have been applied on BMMPAs for perfect absorption. Elbahri and co-workers replaced the metallic structure in the MMPA with a nanocomposite (Au/SiO_2, **Figure 9**a,b) resulting in almost 100% absorption over a broad range of frequencies from UV to NIR, as shown in Figure 9c.[11] They found that the fill factor of gold NPs in the composite can significantly influence the optical response. A 40% filling factor has been found to be optimum for high absorption covering the visible to NIR region, making the surface appear black. This broadband absorption is due to two factors: impedance matching in the MM as well as dipole–image interaction and broad Mie resonance of NPs with a large size distribution. Afterward, they demonstrated a Cu-PTFE nanocomposite BMMPA which presents an average absorption in the visible frequencies above 97%, as shown in Figure 9d.[80] The absorption properties of this copper perfect absorber are greater than that of its gold counterpart because copper is more lossy than gold in the visible spectrum. Although the effect of filling factor and thickness of the film or composite of a silver perfect absorber shows the same influence on the optical properties than in the copper or gold systems, there is an absorption dip at higher frequency for the Ag nanocomposite MMPA, rooted in the overlap of SPR and plasma frequency, as shown in Figure 9e.[116] Due to the high optical absorption in the deep UV region, the Ag nanocomposite BMMPA can be used for UV protection applications. In 2017, a BMMPA with a flexible moth-eye PDMS substrate was obtained by simply replicating patterns of commercial U-shaped anodic aluminum oxide templates, yielding a high absorption of 95.8% ranging from 350 to 1000 nm.[118] Recently, conductive carbon black conductive polymer composite was adopted to obtain BMMPA. Filled with PE, the BMMPA showed a broadband compatible multispectral absorption for visible (300–780 nm, >95%), NIR (780–2400 nm, ≈95%), and microwave bands (2.35–18 GHz, ≈96.8%).[120]

In summary, the absorption peak position and intensity can be engineered by altering the type of nanocomposite, its filling factor, surrounding dielectric environment, and the different layer thickness. The advantage of nanocomposite BMMPAs is their high absorption, obtained through a facile and scalable fabrication process, without involving complex photolithography and pricy electron beam lithography (EBL). Additionally, the absorption is polarization-insensitive and strongly angle independent. However, their working frequency is confined to the UV, visible, and NIR regions due to the plasmonic properties of metal NPs. Inspired by biological systems, researchers can seek solution from nature. Bio-nanocomposites are incorporated to develop BMMPAs. A smart plasmonic absorber based on metal-polymer bio-nanocomposites mimicking beetle's body parts achieves a broadband absorption extending from 300 to 900 nm.[121] Future work should be focused on two points: high-temperature-resistant BMMPAs and low-frequency BMMPAs based on nanocomposites. Due to the high absorption from UV to NIR regions, BMMPAs with nanocomposites are attractive for solar energy harvesting. Dielectric materials of nanocomposites are typically composed of polymers which are vulnerable to high temperature. Extending absorption to the THz region is also another direction of research. Composites with polymer and carbon particles, with large aspect

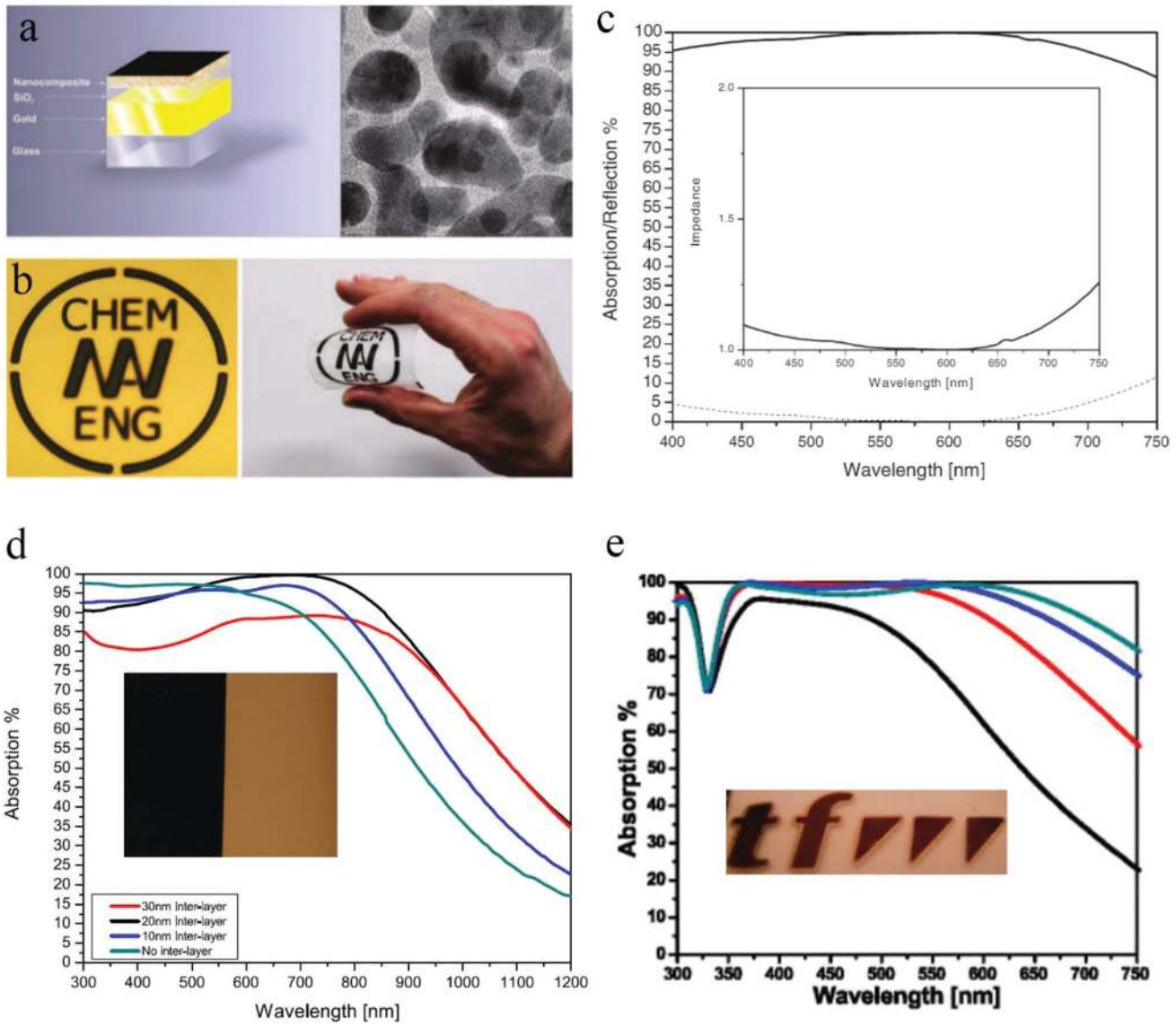

Figure 9. a) Schematic of a perfect absorber structure manufactured by sputtering. The thickness of the nanocomposite, SiO_2 spacer, and gold mirror layers are 20, 25, and 100 nm, respectively. The left panel illustrates that the whole structure sits on top of a glass substrate; the right panel shows a top-view TEM image of the nanocomposite film. b) Perfect absorber (blackbody) coated via mask on gold-coated glass (left) and flexible polymer foil (right). These examples show the potential of the coating for application on different substrates, including flexible ones. c) Absorption (solid line) and reflection (dashed line) spectra of the system described in panel (a), measured at 6° angle of incidence. The inset shows the impedance data of a 20 nm Au/SiO_2 nanocomposite deposited on a 100 nm gold film with 25 nm SiO_2 spacer layer. d) Absorption spectra of 20 nm Cu-PTFE composite on a PTFE spacer layer with different thicknesses, over 100 nm of Cu. The green curve shows the composite on a base layer without any interlayer for comparison. The inset is the photo of the perfect black absorber (left) in comparison with bare copper film (right). e) Absorption spectra of a silver-SiO_2 nanocomposite of 15 nm (black curve), 20 nm (red curve), 25 nm (blue curve), and 30 nm (green curve) thickness, deposited on 15 nm of SiO_2 coating a silver mirror. The inset is true color photograph of the perfect absorber coated on transparent polymeric substrate presenting the logo of Faculty of Engineering (TF) of University of Kiel. (a–c) Reproduced with permission.[11] Copyright 2011, Wiley-VCH. (d) Reproduced with permission.[80] Copyright 2012, Springer Nature. (e) Reproduced with permission.[116] Copyright 2014, AIP Publishing.

ratio, have exhibited absorption properties in the THz[122] and/or GHz[123] region.

2.4. Other BMMPA Designs

In the previous subsection, we have reviewed mainstream approaches to extend the bandwidth of MMPAs, including horizontal and vertical stacking of resonators, introduction of lumped elements and plasmonic nanocomposite BMMPAs. Additional design tools or methods, such as CMM structures,[36,42] space-filling,[69] dielectric tailoring,[89,124,125] using crossed trapezoidal resonators,[24,126] and resonator material tailoring[67,71,81,127,128] are also being investigated to achieve broadband absorption.

2.4.1. CMM Structures

A trilayer CMM absorber structure, fabricated with complementary metal-oxide-semiconductor (CMOS)-compatible materials, combines electrical and cavity resonance mechanisms in the NIR region, demonstrating broadband absorption.[36] The cavity and electrical resonances can be tuned by changing the dimension and dielectric thickness. The dual band absorber is then engineered to be at the same wavelength and by merging the two resonant mechanisms broadband absorption is achieved. Using a different approach to CMMs, Cummer and co-workers proposed a BMMPA structure with complementary ELCs and SRRs, as shown in **Figure 10**a.[42] Figure 10b depicts the spectral response of the joint ELC and SRRs which is stronger and broader than that of an individual ELC or SRR. The calculated absorption is 95% at 2.67 GHz with a FWHM bandwidth of 300 MHz. According to ref. [42], the basic concept of broadening bandwidth of ELC-SRR BMMPAs relies on tailoring the electrical Lorentzian response in ELC and Lorentzian-shaped resonant magnetic response in SRR. This ELC-SRR structure can be further stacked to demonstrate peak absorption of 99.9% at 2.4 GHz, with FWHM of 700 MHz.[42]

2.4.2. Space-Filling Resonator Design

The disadvantage of placing resonators with different sizes in a plane is that it is extremely difficult to fit many different sizes of arrays into one unit cell. Moreover, a unit cell with different resonators, or with the same resonators geometries in different sizes, will give rise to inhomogeneous characteristics, that is, polarization-dependency and sensitivity to oblique incidence.[54] To overcome these problems, Mayer and co-workers used a genetic algorithm (GA) optimization technique to identify the geometry of a single-layer metal nanostructure array that offers broadband absorption independent of polarization, as shown in Figure 10c,d.[69] The nanostructures obey certain predefined fabrication constrains, with a cross dipole centered in the unit cell, a large loop centered and interconnected in the unit cell, and four smaller isolated loops located at the corner of the unit cell. The predefined structures create EM resonances with narrowly spaced center wavelengths which are merged into a broad resonance in the mid-IR region. The measured absorptivity of the BMMPA for unpolarized TE, and TM illumination agrees well with simulation results, as plotted in Figure 10e,f. The average absorptivity of the BMMPA is greater than 98% in a band covering from 1.77 to 4.81 μm. Additionally, optimized Au and Pd structures are compared, showing that the Pd offers significant advantages for robust and reproducible fabrication. While increasing the Au film thickness to 11 and 12 nm results in large fluctuations in absorptivity and a reduction of absorption near the long wavelength edge, increasing Pd thickness from 30 to 40 nm has a negligible influence on the absorption, with only a slight reduction in the long-wavelength extreme. Similarly, a Hilbert space-filling curve, a continuous fractal space-filling curve first described by the German mathematician David Hilbert, has been proposed as a design to provide broadband absorption. A terahertz BMMPA based on resistive Hilbert curve array is proposed for broadband terahertz detection.[129] The structure in this reference differs from the conventional Hilbert curves, in that it uses resistive curves while in the case of traditional Hilbert curve absorbers, the material used is highly conductive. It achieves a fractional bandwidth (bandwidth of a device divided by its center frequency) of 100% for normal incidence and more than 90% in case of oblique incidence of 45° and 60° for both TE and TM polarizations.

2.4.3. Dielectric Layer Tailoring

Broadband absorption can also be achieved by tailoring dielectric layers via mechanical means,[124] temperature changing,[89] applied electric,[15] and magnetic field.[125,130] In our previous study, we demonstrated a BMMPA with pseudo-broadband spectrum by using mechanical means.[124] The top resonator is a typical ELC structure, as shown in **Figure 11**a. By placing a dielectric slab in close proximity to the subwavelength structures, on the condition that this placement leads to symmetry breaking of the overall structure, multiple absorption peaks can be created and the absorption region can be broadened by bringing a vertical half-slab (not shown in figure) or horizontal half-slab (shown in Figure 11b,c) close to it. Distilled water has a frequency-dispersive permittivity, which can be seen as a good candidates for broadband absorption.[89,131] Qu and co-workers used water as the dielectric substrate for broadband absorption, as demonstrated in Figure 11d.[89] In contrast to the well-known metal–substrate metal configuration, the substrate is a hybrid of water and a low-permittivity material. The broadband absorption benefits from the dispersive permittivity of water in the corresponding band. Although the absorption efficiency is weak due to the impedance mismatch stemming from the large permittivity of water, it can be enhanced by introducing a layered performance matching (LPM) layer and top square resonators. Figure 11e,f plots the simulation and measured results of the BMMPA at different temperature, indicating the absorption performance of the water-substrate absorbers could be tuned according to the environment temperature.

Recently, a combination of ferrite and continuous wire forming a MM structure was shown to achieve a tunable negative index.[132] Under an external applied magnetic field, the ferrite offers a broadband magnetic response which interacts with the electric resonance supported by the continuous wire, which is embedded in the ferrite layer. We also demonstrated dual, multiband, and broadband absorption in MMPA based on ferrite in our previous work.[125,133] For broadband absorption, the proposed structure included a copper wire embedded in a FR4 layer and then sandwiched between two ferrite slabs, as illustrated in **Figure 12**a.[125] To excite magnetic anisotropy, a magnetic field is applied to the ferrite slabs along the *z*-direction. Under a different magnetic field, varying from 2.6 to 3.4 kOe, the magnetic resonance shifts from 10 to 12.5 GHz, with a well-preserved large magnetic loss. As a result, absorption is high, while bandwidth and maximum absorption are not changed under the different magnetic field, as shown in Figure 12b.

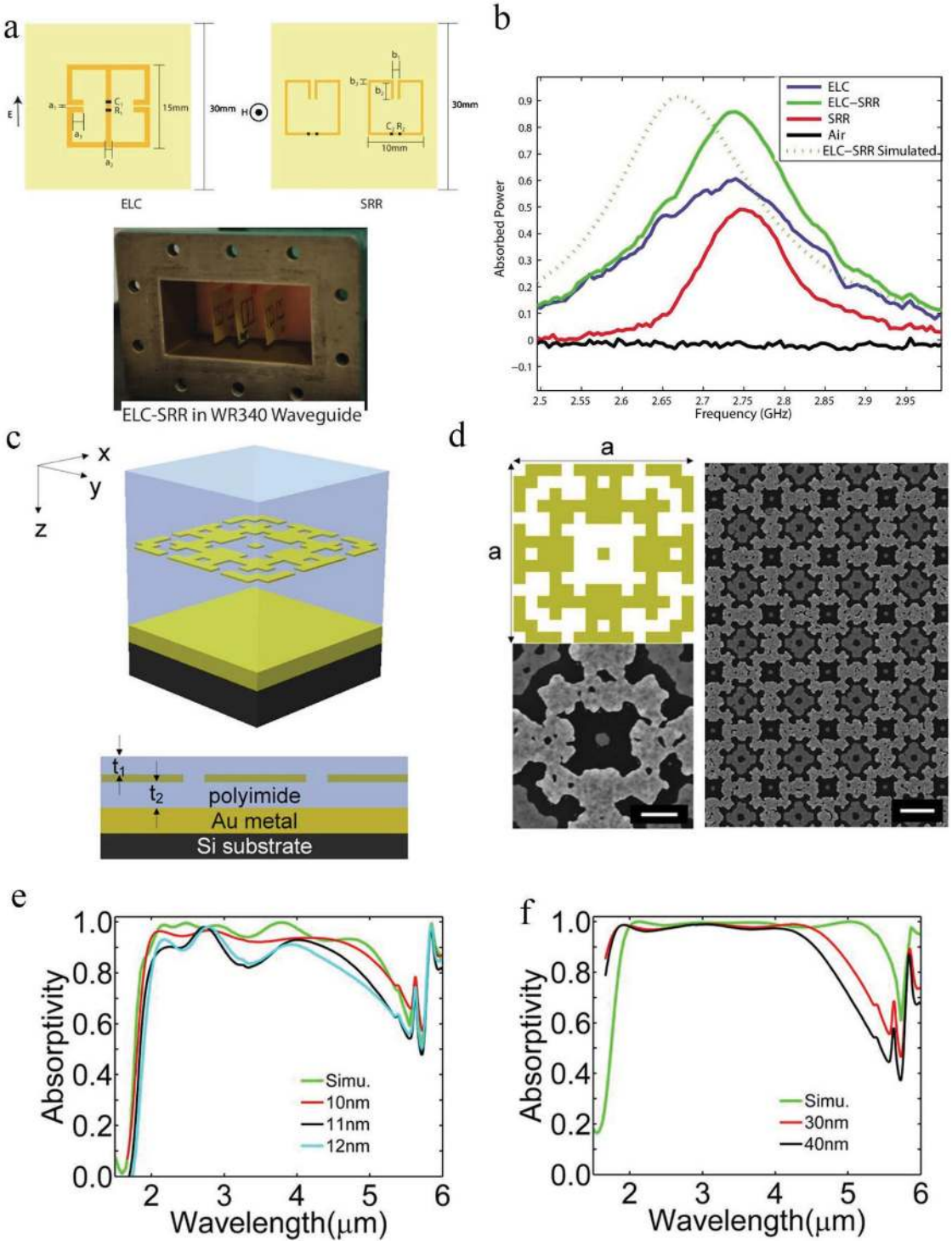

Figure 10. a) The optimum single-cell ELC-SRR absorption was achieved with ELC parameters of $a_1 = 0.35$ mm, $a_2 = 1$ mm, $a_3 = 0$ mm, $C_1 = 10$ pF, and $R_1 = 10\ \Omega$, SRR parameters of $b_1 = 0.7$ mm, $b_2 = 3$ mm, $b_3 = 0.5$ mm, $C_2 = 10$ pF, and $R_2 = 5\ \Omega$ and ELC-SRR measured in a WR340 closed waveguide. b) ELC-SRR has the highest and broadest absorption with a 86% peak at 2.74 GHz, and FWHM bandwidth of 170 MHz. c) Diagram of optimized Au-based BMMPA structure. d) Top left: Top view of one unit cell of the design. Bottom left: FESEM image of a unit cell of the fabricated structure. Scale bar is 200 nm. Right: Low-magnification FESEM image of the same structure. Scale bar is 600 nm. e) Simulation and measurements for Au-based BMMPA under unpolarized illumination at normal incidence. The average Au thicknesses of the Au nanostructures as determined by atomic force microscopy measurements are 10, 11, and 12 nm. f) Simulation and measurements for Pd-based MMAs with Pd nanostructure thicknesses of 30 and 40 nm under unpolarized illumination at normal incidence. (a,b) Reproduced with permission.[42] Copyright 2010, AIP Publishing. (c–f) Reproduced with permission.[69] Copyright 2014, American Chemical Society.

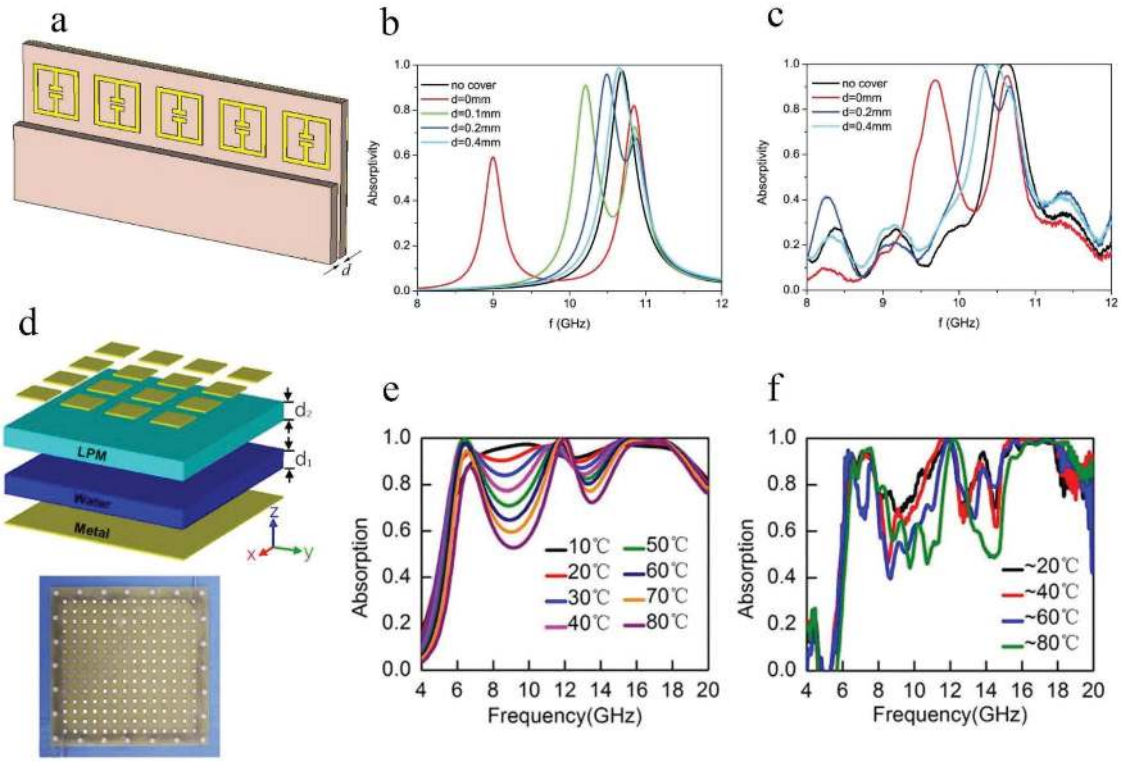

Figure 11. a) BMMPA with a horizontal half-slab; b) theoretical and c) experimental absorption spectra for different *d*. d) 3D schematic diagram of the water-substrate BMMPA and optical image of the assembled prototype of the water-substrate BMMPA; e) simulated and f) measured absorption spectra of the fabricated water-substrate BMMPA at different temperatures. (a–c) Reproduced with permission.[124] Copyright 2012, Optical Society of America. (d–f) Reproduced with permission.[89] Copyright 2017, AIP Publishing.

2.4.4. Crossed Trapezoidal Resonators

For applications in the next generation of electronic devices for photovoltaics,[24,134] photoelectrochemical water splitting,[135] photodetectors,[30] and thermal engineering,[136] there is a need to address the requirement of reducing fabrication complexity and material consumption. Ultrathin BMMPAs based on crossed trapezoids have been theoretically and experimentally demonstrated.[24,126] Aydin et al. proposed ultrathin planar plasmonic superabsorbers composed of crossed trapezoidal arrays that are capable of absorbing light from 400 to 700 nm with a measured average absorption of 71%,[24] as shown in Figure 12c–e. While a different transversal resonance is excited at each width along the trapezoid under TE polarization, broadband extinction for TM polarization is rooted in the resonant electromagnetic responses of different cross sections of the trapezoids at different wavelengths. Therefore, these BMMPAs have the potential of leveraging their optical properties to address the intrinsically weak absorption of ultrathin nonstructured materials when realizing superabsorbers with atomic-scale control.

2.4.5. Resonator Material Tailoring

BMMPAs can be fabricated with resonators made of low bandgap materials, highly lossy metals, MXene, or coupling them with epsilon-near-zero (ENZ) materials. A 50 nm thick BMMPA structure with a Ge (low bandgap) nanobeam on the top demonstrated broadband absorption from 400 to 900 nm, as shown in **Figure 13**a,b.[137] Since noble metals in MMPA, for example, Au, Ag, and Pd, usually create narrow absorption peaks, they can be replaced by highly lossy metals to achieve broadband absorption, such as W, Cr, Ni, or Ta. For instance, we reported a narrow-band MMPA based on Au rings operating in the near and far-infrared regions,[22] while another group reported a BMMPA with broadband absorption higher than 90% from 1.00 to 2.43 THz by using highly lossy Cr rings.[71] Due to the coupling between the gap plasmon mode of a metasurface and an ENZ mode in the nanoscale ITO film, a BMMPA with an ENZ material has shown a broadband and perfect absorption resonance. The system, depicted in Figure 13c,[128] incorporates a 12 nm thick ENZ ITO layer between the patterned gold nanodisks and the SiO_2 layer, and shows a 240 nm broadband, flat-top perfect (>98%) absorption centered at 1550 nm, while the traditional MMPA demonstrated only a narrow absorption, as shown in Figure 13d. Plasmonic resonances in nanostructured $Ti_3C_2T_x$ MXene, where T_x represents surface functional groups, have been manipulated to achieve absorption over a broad bandwidth of ≈1.55 µm, as shown in Figure 13e,f.[81] This can be attributed to strong LSPRs at near-infrared frequencies and the optical losses inherent to $Ti_3C_2T_x$.

In this section, we have first reviewed the mainstream methods used to achieve broadband absorption operating from UV to microwave frequencies. By integrating differently sized resonators on the *xy*-plane, the absorption bandwidth

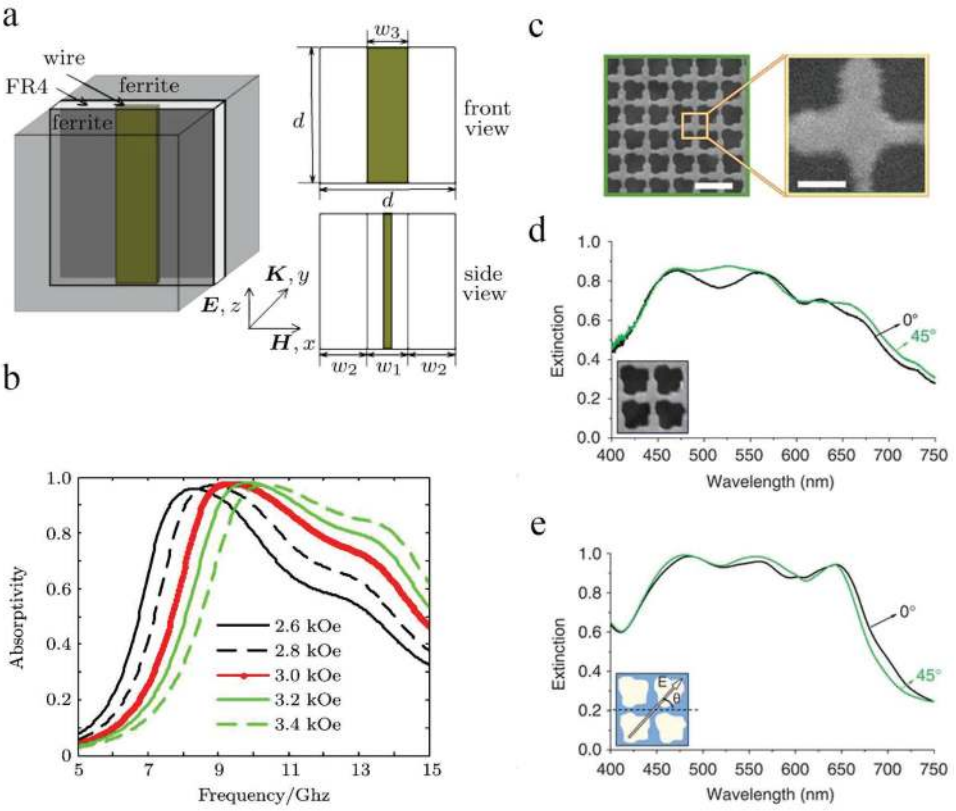

Figure 12. a) Schematic diagram of the ferrite-wire BMMPA unit cell. Front view, side view, and structure parameters are presented. b) The absorption bands under different magnetic biases. c) SEM image of the fabricated crossed trapezoidal arrays (left) and a single unit cell (right). Scale bars are 500 and 100 nm, respectively. d) Measured and e) simulated extinction spectra using digitized SEM images (inset) for different incident electric field polarization angles (inset). (a,b) Reproduced with permission.[125] Copyright 2012, IOP Publishing. (c–e) Reproduced with permission.[24] Copyright 2011, Springer Nature.

widens as the number of distinctly sized resonators increases. Another advantage is that the broadband absorption can be tuned as the size changes. However, due to the relatively small cell size required to obtain large enough densities of each resonator, the number of resonators that can be incorporated within the same unit cell is limited. Therefore, the broadening effect based on this type of integration is, to some extent, limited to a finite bandwidth. In comparison, vertical stacking of the resonators does not have a limitation on the number of integrated resonators. Hence, their absorption bandwidth can be much broader, although there is a trade-off between thinness and the bandwidth of the absorber. Intuitively, absorbers with more layers require complicated fabrication steps and the use of complex fabrication tools. Nevertheless, by exploiting slow light effect ultrathin layers that do not individually support localized resonances can be stacked relatively easily. Lumped elements can be welded into MMPA to lower their *Q*-factor in the GHz region; however, they are not feasible for THz, IR, or optical frequencies because the resonator size is in the nanoscale. Nanocomposite BMMPAs can be fabricated by facile coating and sputtering; however, their broadband absorption is limited to UV, visible, and NIR. Besides, broadband absorption can be achieved by adopting CMM structures, space-filling, dielectric material tailoring, crossed trapezoidal resonators, and through the material tailoring of the top resonators. To summarize this section, we have compiled two tables. **Table 2** compares advantages and disadvantages of the four main methods discussed above, including fabrication methods, operating frequency, cost, polarization-dependence, and fundamental limitations; **Table 3** compares different methods of BMMPA design, including data on the reported FWHM, operating frequency, resonator shape/material, dielectric material, average absorption; only a few representative references are cited in the table.

3. Applications of BMMPAs

The last decade has witnessed a proliferation of BMMPAs for diverse applications, including solar PV, photodetection, bolometry, and the manipulation of mechanical resonances. Compared with their traditional counterparts, they have shown superior properties such as polarization-independence, insensitive to incidence angle, and perfect absorption with tunability and broader bandwidth. Benefiting from advanced, cost-effective micromachining technology, BMMPAs can be further applied to devices based on photoacoustic, photoelectric, photothermal, and photomagnetic effect. In the subsections that follow, we will review specific examples of applications for BMMPAs.

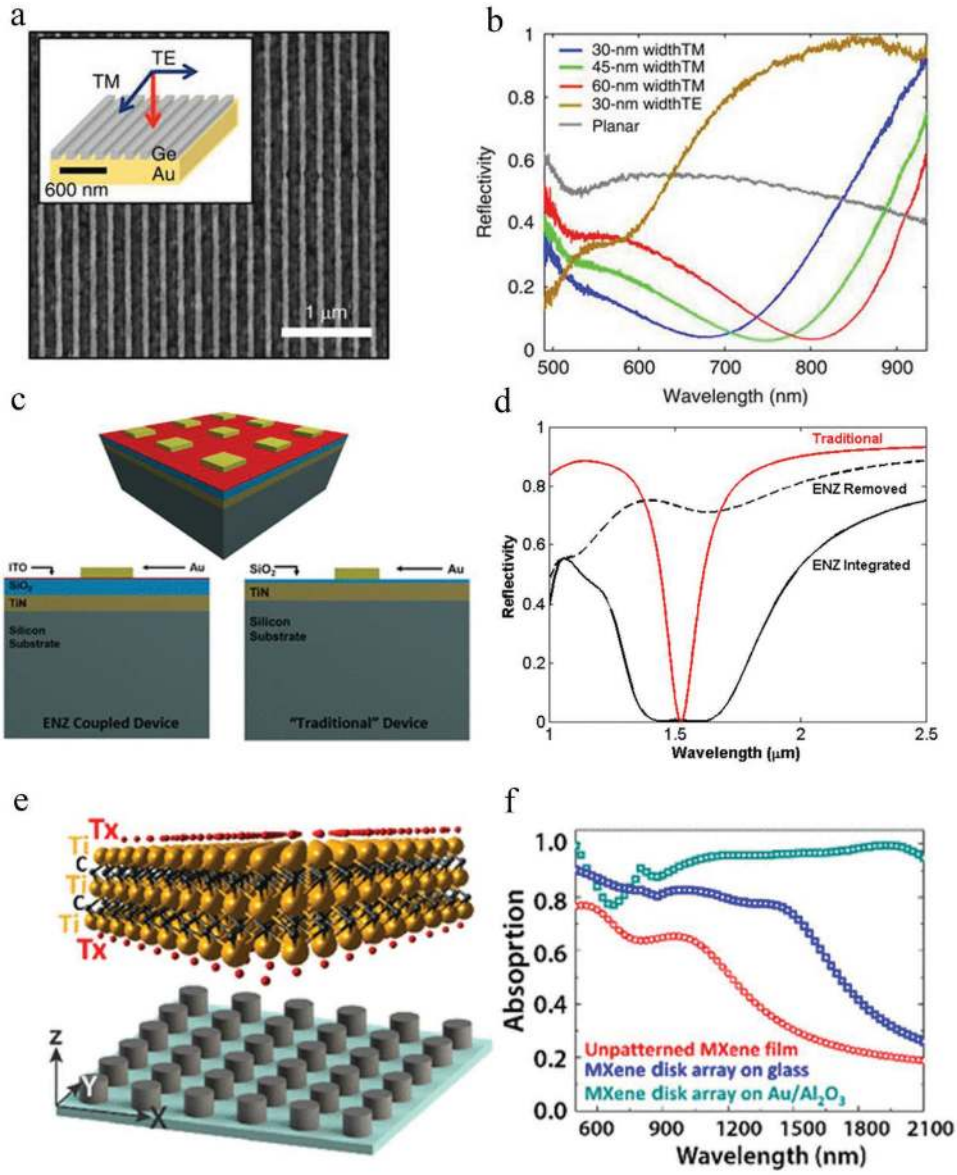

Figure 13. a) Top-view SEM image of a fabricated metafilm with Ge beams, with a 200 nm period and 0.3 duty cycle. Scale bar: 1 μm. b) Measured reflectivity spectra for TM polarized light for metafilms constructed from nanobeams with a width of 30 (blue), 45 (green), and 60 nm (red). The reflectivity spectra for TE polarized light of the array with 30-nm-wide beams (brown) and a planar Ge film (grey) are shown for reference. c) Schematic (top) and cross section of the device consisting of a TiN metallic thick film, a SiO_2 dielectric layer, an ITO nanofilm, and a patterned periodic array of metal squares, all on top of a Si substrate, and a schematic of a reference "traditional" perfect light absorber without an ENZ layer. d) Simulated reflectivity curves for a perfect absorber with integrated ENZ (solid black line), absorber without ENZ layer (dashed black line), and an optimized "traditional" gap-plasmon perfect light absorber without ENZ layer (solid red line). e) Schematic of the BMMPA fabricated using 2D titanium carbide ($Ti_3C_2T_x$) MXene. f) Comparison of experimental absorption spectra of the two types of disk arrays and unpatterned MXene film (incident light is TE polarized; angle of incidence is 20°). (a,b) Reproduced with permission.[137] Copyright 2015, Springer Nature. (c,d) Reproduced with permission.[128] Copyright 2018, American Chemical Society. (e,f) Reproduced with permission.[81] Copyright 2018, American Chemical Society.

3.1. BMMPAs for Solar Photovoltaics

Solar PV systems are considered as ideal candidates to harvest solar radiation. As commercial PV devices approach the detailed balance limit, the requirement for cost-effective solar cells is to achieve high efficiency with less material consumption. In the past decades, light trapping schemes were proposed to enhance the light absorption of solar cells.[114,138] However, their intrinsic defects hinder their large-scale production, for example, degradation of open-circuit voltage of quantum dots solar cells,[114] or surface recombination of nanowire solar cells.[139] The current thin film PV systems need less material, but their disadvantage lies in reduced absorption due to the thinner absorber layer. Hence, light trapping schemes are critical for thin film solar cells. Details for light trapping techniques, along with the working principles and physics of PV cells are given in refs. [139,140]. The light

Table 2. Properties of four main BMMPAs, including mechanism, operating frequency, available fabrication techniques, cost, polarization-dependence, and fundamental limitation.

Method	Mechanism	Working frequency	Fabrication	Cost	Polarization-dependence	Limitation
Horizontal integration	Multiple resonances	UV to GHz	EBL or photolithography	High or low	Resonator shape dependence	Limited bandwidth
Vertical stacking	Multiple resonances or slowlight waveguide modes	UV to GHz	RIE or mechanical milling	High or low	Resonator shape dependence	Thick
Welding lumped elements	Reduce *Q*-factor	GHz	Photolithography and welding	Low	Resonator shape dependence	Only GHz and bulk
Using nanocomposites	Plasmonic effect	UV to NIR	Sputtering or coating	Low	Polarization insensitive	Low stability

trapping ability of BMMPAs can be applied to both solar thermophotovoltaic (STPV) devices and ultrathin solar cells.

The main challenges in direct utilization of plasmonic resonance absorption of solar energy in the visible range are significant Ohmic losses and their consequential heating. An attractive route to avoid the adverse consequences of plasmonic overheating from direct visible absorption is to utilize STPVs, as shown in **Figure 14**. STPV is a conversion process from

Table 3. A summary of methods used to create BMMPAs; NR is not reported and NA is not applicable in the table.

Methods	FWHM	Operating frequency	Resonator shape	Resonator material	Dielectric material	Average absorption [%]	Ref.
Horizontal integration	2.16 μm	3–5 μm	Cross	Gold	SiO_2	≥50	[62]
	1.15 THz	6.24–7.04 THz	Square	Copper	SiO_2	≈90	[64]
	2.8 GHz	9–13 GHz	Circle	Copper	Epoxy glass	≥95	[91]
	NR	0.5–0.7 μm	Square hole	Gold	SiO_2	>95	[96]
	NR	9.79–11.72 GHz	Dendritic	NR	FR-4	≥90	[59]
	NR	8.3–17.4 GHz	Windmill	ITO	PET and PMMA	≥90	[73]
	NR	0.65–1.45 THz	SRR and disk	Gold	PDMS	≥80	[94]
	5.66 GHz	12.38–22.28 GHz	SRR and SMP	Copper	FR-4	≥60	[86]
	10.1 THz	31.0–37.0 THz	Circle	Gold and graphene	Polyimide	≥90	[75]
Vertical stacking	2.3 GHz	8.8–10.8 GHz	Ring	Copper	FR-4	≥80	[99]
	1.72 μm	3.0–5.5 μm	Sawtooth slab	Gold	Germanium	≥95	[82]
	NR	8.37–21 GHz	Loop	Copper	TMM4	≥90%	[90]
	2.40 THz	4.08–5.94 THz	Cross	Gold	Polyimide	≥60	[93]
	NR	8–100 THz	Frustum pyramid	Graphene	$n = 3^{1/2}$	≈90	[78]
	NR	46.2–62.8 μm	Ribbon	BP	$n = 1.7$	≥90	[79]
	≈9 THz	4–12 THz	Asymmetric void	Graphene	$n = 2.5^{1/2}$	≥90	[105]
Welding lumped elements	700 MHz	2.2–3.0 GHz	ELC-SRR	Copper	FR4	≥60	[42]
	1.38 GHz	3.1–5.6 GHz	Split-coin	Copper	FR4	≥90	[45]
	>4.56 GHZ	8.87–16.47 GHz	Double-circle ring	Copper	FR4	≥90	[44]
	NR	7.93–17.18 GHz	Double octagonal rings	Copper	PEC	≥90	[109]
	NR	8.45–9.3 GHz 9.2–10.45 GHz	Jerusalem-cross	Conductor	FR4	≥90	[112]
Using nanocomposites	NR	400–2500 nm	NA	Ag NPs	Teflon AF	≥60	[119]
	NR	Visible range	NA	Au NPs	SiO_2	≈100	[11]
	NR	Visible range	NA	Cu NPs	PTFE	≥97.5	[80]
CMM	NR	1.3–2.5 μm	Sheet with square hole	Molybdenum	SiO_2	NR	[36]
GA	NR	1.77–4.81 μm	Mixed shapes	Palladium	Polyimide	≥98	[69]
Fractal space-filling curve	1.3 THz	0.5–1.8 THz	Hilbert curve	Aluminium	$n = 3^{1/2}$	≥90	[129]
Resonator material tailoring	>1.55 μm	500–2500 nm	Disk	Titanium carbide	Al_2O_3	≈90	[81]
Crossed trapezoidal arrays	NR	400–700 nm	Crossed trapezoid	Silver	SiO_2	≥71	[24]
Lossy metal	1.94 THz	1.0–2.43 THz	Ring	Chromium	Polyimide	≥90	[71]

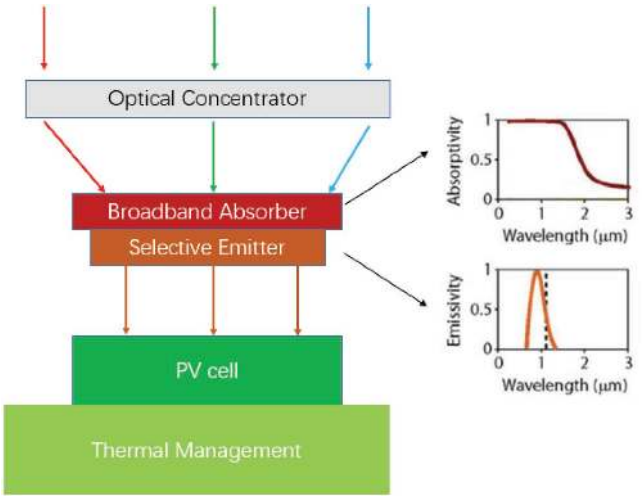

Figure 14. Schematic of STPV systems. The absorber and emitter typically operate above 1000 K while the PV cell operates at room temperature.

heat to electricity via photonic reemission. Due to its broadband absorption ability, a BMMPA can be applied on STPVs to address their poor absorption. The STPV systems have been widely investigated due to the theoretical models that predict up to 85% efficiency.[136] Under a suitable light concentration scheme, and with a reasonable ratio of areas between the emitter and absorber, the efficiency of a STPV system adopting an absorber (tungsten pyramids)–emitter (tungsten slab) pair with a single-junction solar cell can exceed the Shockley–Queisser (SQ) limit.[141] The theoretical limit of an STPV system with solar absorber/narrow-band thermal emitter structures was also calculated to be 41%, which is higher than the SQ limit of 31% at one sun.[12] The efficiency remains above 31% for an emitter temperature (T_e) > 1200 K when a heat reservoir is included in the STPV system design, extending the power-generating period beyond the daytime.

The key design goals in creating an absorber for STPV application are: broadband high absorption covering UV, visible, and NIR region along with zero emittance in the mid-IR regime to minimize energy loss from spontaneous thermal radiation; independence of the angle of incidence and polarization of incoming light. Extensive efforts have been focused on achieving ideal STPVs with BMMPAs. Square rings with four gaps are tailored to obtain polarization angle independent BMMPAs for solar application in the microwave, infrared, and visible regime.[88] Most of the previous designs on MMPAs work at room temperature, but the temperature-dependent optical properties of BMMPA have to be fully investigated in order to understand their thermal dependence while harvesting efficient solar energy. Chou et al. demonstrated a thermally stable selective solar absorber made of 2D metal–dielectric photonic crystal structures after 24 h heating at 1000 °C.[142] Wang et al. experimentally demonstrated a highly efficient MM selective absorber for solar thermal energy harvesting, working at temperatures up to 350 °C.[68] The structure is composed of a 2D Ti grating, MgF_2 dielectric layer, and a tungsten film, depicted in **Figure 15**a–d. Their absorbance within the solar spectrum is higher than 0.9 and a low emittance of 0.2 (not shown in the figure) in the mid-IR regime as shown in Figure 15e. While a black surface could only convert 32% of solar energy to useful heat at 100 °C and would drop quickly to zero at 125 °C, the final solar thermal conversion efficiency of the absorber could reach 78.1% under 1 sun (i.e., no optical concentrator) at 100 °C, monotonically dropping to zero at the stagnation temperature of 241 °C, as compared in Figure 15f. The solar-to-heat conversion efficiency can be further boosted by using concentrators. Figure 15g shows that the measured conversion efficiency of an absorber at 400 °C can reach 21.5% under 5 sun, 57.4% with 10 sun, and 80% with 25 sun.

Noble metals are indispensable in creating BMMPA structures, but they suffer from low melting points. STPV systems usually operate at 800 °C or higher, thus approaching or surpassing the melting points of bulk Au (1063 °C), Ag (961 °C), and Al (660 °C).[143] Ni has a high melting point (1455 °C) but its absorption performance is usually limited. Furthermore, the melting point of the patterned metallic structures at the nanoscale is greatly lowered due to the small size effect.[144] Therefore, refractory metals with high melting points are selected to be used in STPVs, such as tungsten (W, 3422 °C),[143,145,146] molybdenum (Mo, 2623 °C),[146,147] and tantalum (Ta, 3020 °C).[141,148] Using Ta, an integrated double-sided 2D photonic crystal (PhC) absorber/emitter pair is demonstrated for a high-performance STPV systems.[141] At an irradiance of 130 kW m^{-2}, the PhC absorber demonstrates more than a twofold improvement in measured STPV system efficiency (3.74%) relative to a nearly blackbody absorber (1.60%). However, W, Mo, and Ta are not good absorbers in the visible range due to their large impedance mismatch and thus cannot effectively cover the solar spectrum. Li et al. adopted TiN to fabricate a BMMPA with an average absorption of 95% over the range of 400–800 nm after annealing at 800 °C for 8 h,[16] indicating its promise for applications in STPV systems, as shown in Figure 15h–j. On the other hand, an Au absorber is greatly damaged when illuminated under the laser intensity of 6.67 W cm^{-2}, as can be seen from Figure 15k,l. TiN absorber can remain stable under a laser illumination of 6.67 W cm^{-2}, but is somewhat damaged at the illumination intensity of 15.5 W cm^{-2}.

In addition to high thermal stability, another relevant issue for BMMPAs in solar applications is Ohmic loss. Ohmic loss and the resulting material heating lead to a decrease in efficiency.[149] Metallic nanostructures operating at optical frequencies suffer from larger Ohmic losses than those working at lower frequencies, because the geometric skin depth is larger than bulk skin depth and the larger absorption cross section induces strong currents. This is a problem not only facing the STPV systems, but also MM solar cell structures. Güney et al. demonstrate that Ohmic losses in MMs can be reduced by geometric tailoring, such as by increasing the radius of curvature at sharp corners.[150] In this study, the so-called bulk skin depth technique was proposed to reduce the geometric skin depth at optical frequencies to reduce the Ohmic losses by offering three advantages: (1) optical absorption in the metallic structure (i.e., Ohmic loss) is shifted into the semiconductor, with increased optical absorption useful for solar energy conversion; (2) reduced Joule heating; (3) additional interconnections

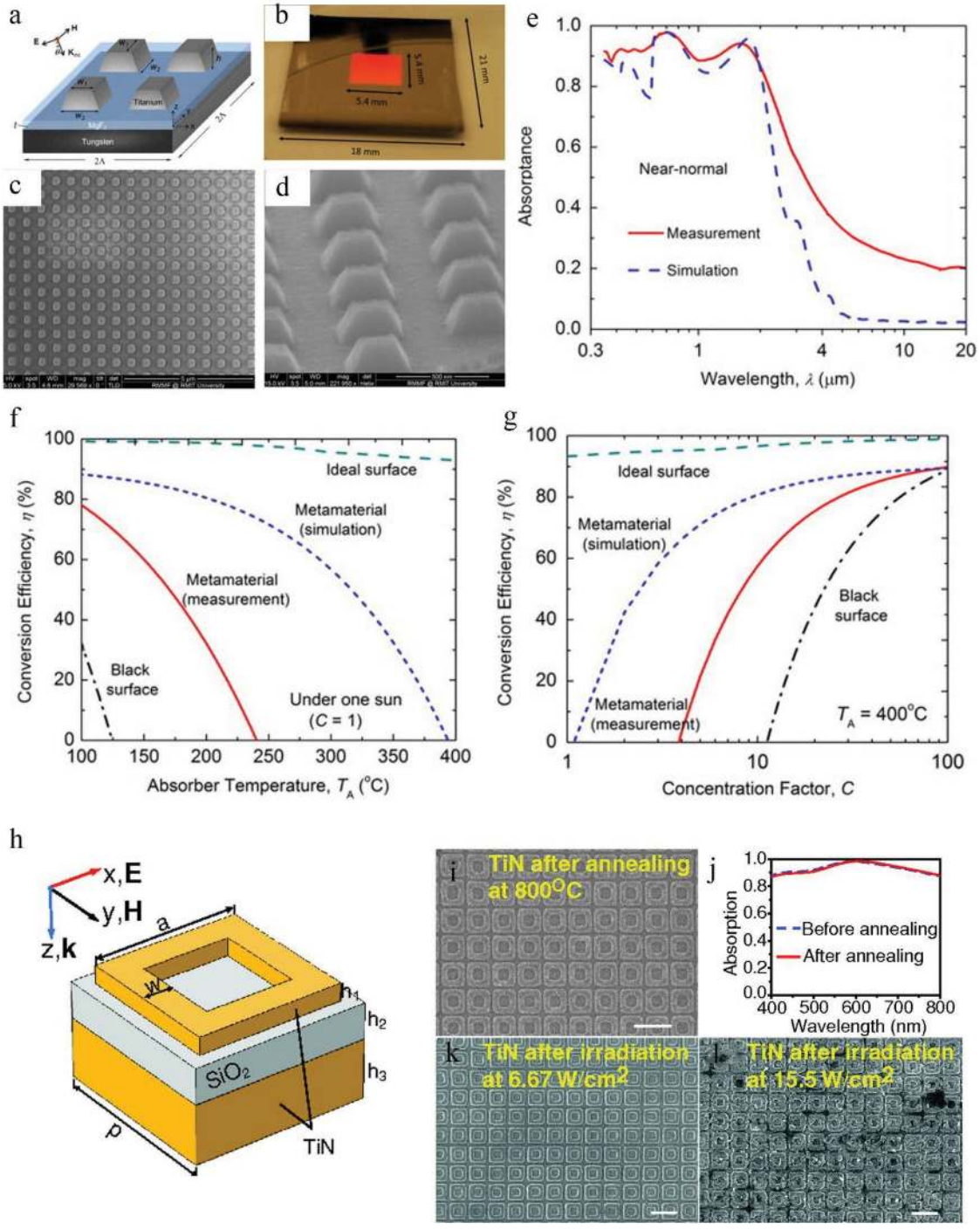

Figure 15. a) Structure schematic for proposed MM solar absorber. K_{inc} represents the incident wavevector, and the incidence angle θ is defined as the angle between K_{inc} and the surface normal. The plane of incidence (POI) is defined as the *xz*-plane. The E field is in the POI for TM incidence, while it is perpendicular to the POI for TE incidence. b) Photo of the fabricated sample for optical characterization. SEM images of the fabricated absorber sample from c) top view and d) side view. e) Measured and simulated room-temperature spectral absorptance of the MM solar absorber. f) Predicted solar-to-heat conversion efficiencies of an ideal selective surface, the MM solar absorber (with optical properties either measured or simulated), and a black surface as a function of absorber temperature absorber temperature (T_A) under 1 sun. g) Solar-to-heat conversion efficiency for all three surfaces as a function of concentration factor C at an absorber temperature of T_A = 400 °C. h) Schematic representation of a unit cell of the three-layer TiN MMPA with dimensions of a = 250 nm, w = 50 nm, p = 300 nm, h_1 = 30 nm, h_2 = 60 nm, and h_3 = 150 nm. i) SEM image and j) the measured absorption of the TiN absorber after annealing at 800 °C for 8 h, as well as the reference measured absorption of TiN before annealing; SEM images for the TiN absorber after being illuminated by a laser with an intensity of k) 6.67 and l) 15.5 W cm^{-2}. (a–g) Reproduced with permission.[68] Copyright 2015, Elsevier B.V. (h–l) Reproduced with permission.[16] Copyright 2014, Wiley-VCH.

can be added in the system without destroying or short-circuiting the absorber.

In conclusion, BMMPAs play a critical role in enhancing absorption for PV applications. The challenge is how to design high-temperature, resistive absorbers while maintaining low Ohmic losses. In addition to the absorber, a narrow bandwidth selective emitter needs to be carefully designed to maximize efficiency.[151] As of today, an efficient solar absorber with both spectral selectivity and high-temperature compatibility is still lacking. Nonradiative decay of surface plasmon in BMMPAs is a parasitic process, but recent studies have shown that it can be harnessed in the form of hot electrons for photovoltaics,[152] photocatalysis,[153] and photodetection.[154] Unfortunately, the quantum efficiency of devices based on hot electrons is still low due to poor electron injection.

3.2. Photodetection with High Responsivity

Recent studies have shown that photodetection can exploit the hot electrons generated from SP or LSPR nonradiative decay, providing a chance for using MMs in photodetection.[30,154,155] In metal–dielectric interfaces, a Schottky barrier is formed, as shown in **Figure 16**. The hot electrons from SP nonradiative decay can be transported to the junction interface, where they can be injected into the band of semiconductor before thermalization if they have enough energy. The bandwidth is limited by Schottky barrier height rather than the bandgap of the semiconductor.[154] If one can obtain a broadband absorption at energies beyond the bandgap of the semiconductor, a broadband photodetector can be realized. Therefore, there are two advantages in using MMPAs as photodetectors: (1) providing hot electrons to detect photons below the bandgap of the semiconductor; (2) enhancing light absorption by incorporating a MMPA with larger light interaction cross sections than the semiconductor.

However, SPs and LSPRs are intrinsically narrow therefore only allowing limited detection bands. Some groups have demonstrated photodetectors based on BMMPA to circumvent the narrow bandwidth. Valentine and Li first demonstrated a BMMPA detector composed of bipartite checkerboard supercell, as shown in **Figure 17**a,b. It maintains absorptivity over 80% from 1250 to 1500 nm, as shown in Figure 17c. A peak absorptivity above 90% is maintained for incident angles of up to 75° and 60° under p- and s-polarized illumination, respectively. Due to the presence of the ultrathin BMMPA structure, the efficiency of hot electron transfer process is significantly enhanced, its FWHM is up to 800 nm and photoresponsivity is larger than 1.8 mA W^{-1} from 1200 to 1500 nm, as shown in Figure 17d.[154] In the same year, Yu and co-workers proposed a new concept for the development of a BMMPA photodetector in the telecommunication region: deep-trench/thin-metal (DTTM) active antenna structures that enhance the photoresponsivity of Si beyond the band edge, as shown in Figure 17e.[30] The peak value of absorbance for the DTTM arrays (88%) was four times and one order of magnitude larger than those of nanoantennas and dot/hole arrays, respectively, as compared in Figure 17e. The photoresponsivity curves demonstrated higher responsivities in the shorter wavelength regime, gradually decreasing when increasing the wavelength of the incident light, as shown in Figure 17f. Distribution of photocurrents to reconstruct an image of the letters "NTU," are shown in Figure 17g, as recorded at an intensity of 1.2 fW μm^{-2} at a wavelength of 540 nm, 4.7 pW μm^{-2} at a wavelength of 1310 nm, and an intensity of 4.57 pW μm^{-2} at a wavelength of 1550 nm, respectively. Therefore, Si-based DTTM devices displayed excellent ability for photodetection beyond the bandgap of Si.

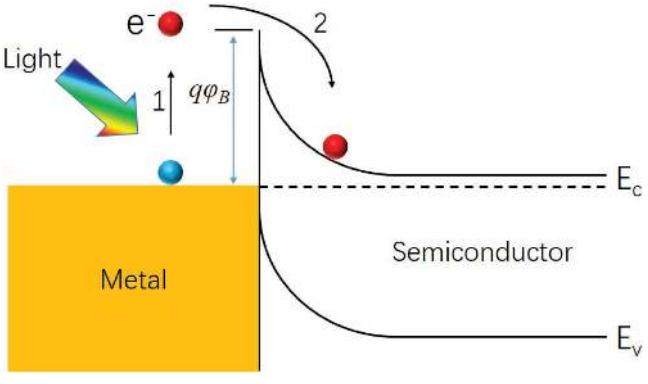

Figure 16. Energy band diagram for plasmonic hot electrons over a metal–semiconductor Schottky barrier, $q\phi_B$.

The excitation of hot carriers through plasmonic effects is a very fast process,[157–159] thus offering an additional advantage for the creation of high-speed photodetectors. Importantly, the generation rates of these nonthermal carriers (**Figure 18**a) can be greatly increased by enhancing the electric field in the metal structures. Regions with large field enhancement (hot spots), generated either by the geometry of specific nanoantennas[158,160] or by the near-field interaction of neighboring structures,[157,158] drive larger rates of generation of hot carriers. Figure 18 shows selected results from two different studies that illustrate these two characteristics of the generation of hot carriers: the ultrafast nature of their excitation and the relevance of the hot spots in exciting them. These studies employ pump-probe measurements to study the carrier dynamics in MM composed of Au nanodisks[157] or Au and Ag NPs[158] on top of a gold layer, separated in both cases by a dielectric spacer layer of various thicknesses. The spacer thickness changes the intensity of interaction between the top nanostructures and the gold layer. Thinner spacers increase the field enhancement in the system and give rise to hot spots, as the simulation results shown in Figure 18c,d. When this occurs, highly nonthermal hot carriers are generated in high densities, creating a strong fast transient signal that attenuates very rapidly as the carriers thermalize. This can be seen in Figure 18b,e.

Enhanced generation of hot carriers through plasmonic excitation depends on the intensity of electric field in the metal, thus the importance of hot spots and small sizes,[157,161,162] but especially at the surfaces of the NPs or films. This is not only to facilitate their injection through the Schottky barrier, a point discussed below, but also to directly increase the rate of generation of hot carriers by surface effects. These constrain the coherent excitation of the electron cloud in the plasmon, inducing electron–surface collisions with transitions that do not conserve linear momentum of an electron.[161,162] The relevance of the NP surface in this process highlights the importance of its geometry, which can generate intense hot spots

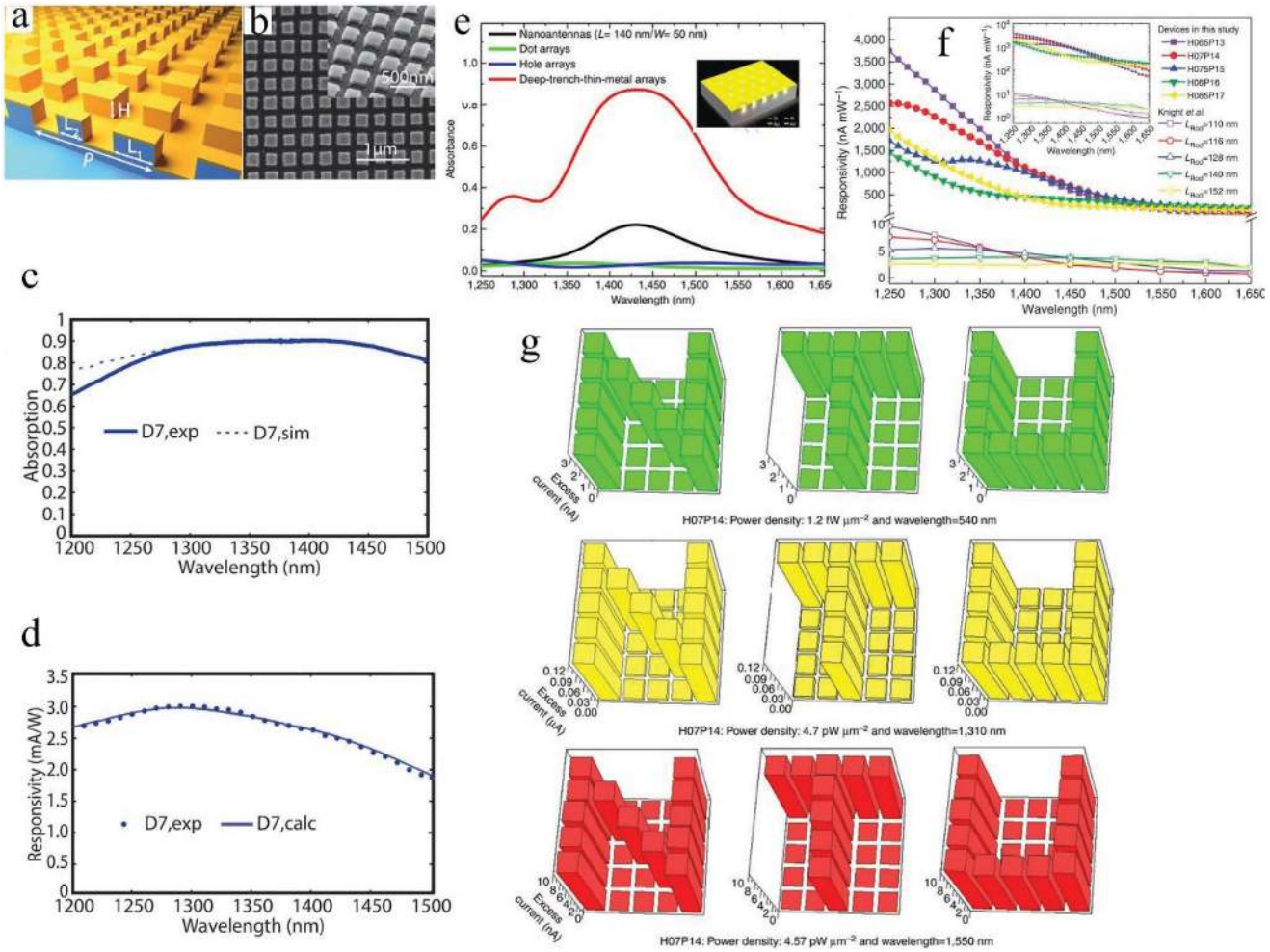

Figure 17. a) Schematic of the BMMPA photodetector. The dimensions of the photodetector are $L_1 = 185$ nm, $L_2 = 225$ nm, $P = 680$ nm, $H = 160$ nm. b) SEM image of the fabricated device. c) Experimentally measured (solid) and simulated (dashed) absorption spectra of the BMMPA detector. d) Experimentally measured (circles) and calculated (line) photoresponsivity spectra of the BMMPA photodetector. e) Simulated absorption spectra of the four types of antenna structures. Among them, the DTTM arrays exhibited the largest absorption in the broadband regime. The inset is the illustration of the detector structure. f) Responsivity spectra of the proposed DTTM devices, in comparison with the nanoantenna-based devices reported by Knight et al.[156] g) Bar charts displaying excess current obtained by the H07P14-containing DTTM device under an applied bias voltage of 0 V, detected at wavelengths of 540, 1310, and 1550 nm. The images were constructed based on the existence or absence of a photocurrent during the point-by-point scanning of the DTTM device. Clear images of the capitalized letters "NTU" were obtained, even though the incident power density was low; in particular, 4.7 pW μm^{-2} at a wavelength of 1310 nm and 4.57 pW μm^{-2} at a wavelength of 1550 nm. The pixel size is 5 mm. (a–d) Reproduced with permission.[154] Copyright 2014, American Chemical Society. (e–g) Reproduced with permission.[30] Copyright 2014, Springer Nature.

without the need for interparticle interaction by adding sharp features or tips, such as in nanostars or nanocubes.[160,162–164] Furthermore, small NPs have a larger surface-to-volume ratio, thus offering higher relative generation rates of hot electrons.[162,164] Although small NPs by themselves may not provide a wide spectral interaction profile, they can be used to sensitize an ensemble of larger resonators in interaction, or in a polydisperse and interacting sample.[165]

A variety of different photodetector designs use hot carriers generated by plasmonic excitation,[30,154,166] including the combination of metal antennas with 2D materials serving as a collecting layer for the exited carriers.[167] A recent example of a planar BMMA that takes advantage of the hot spot effect is presented by Wen et al., who covered a disordered planar collection of Si nanoholes (SiNH) with a thin layer of Au,[168] as depicted in **Figure 19**a. In this system, besides the excitation of modes resonant on the cavities of the top layer, the interhole interaction promotes excitation of electrons through hot spots, as illustrated in Figure 19b,c, which show the simulated electric field distribution. With this approach, they achieved absorptions greater than 80% across a bandwidth of ≈1 μm (wavelengths from 1100 to 2000 nm), as shown in Figure 19d, due in part to the variety of sizes of the nanoholes on the surface. At the same time, this irregular planar layout makes the device strongly polarization-independent. This stands in contrast with most of the designs discussed in this review, which typically have periodic patterns. Another example of this kind of design has been reported by Lu et al., showing a hot electron photodetector with a collection of polydisperse gold NPs separated from a gold film by a TiO_2 spacer, as shown in Figure 19e, effectively covering

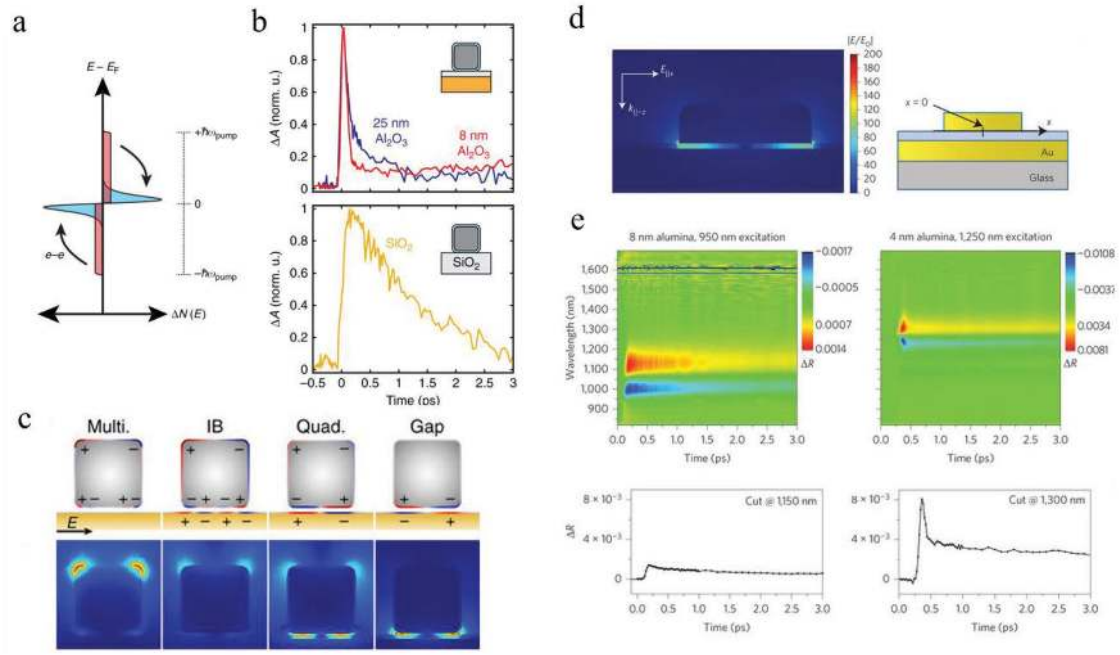

Figure 18. a) Hot electron distribution from plasmon excitation. Nonthermal (red) carriers initially form a symmetric stepwise distribution relative to the Fermi energy upon excitation. After electron–electron scattering, a thermalized electron population (cyan) with a Fermi–Dirac distribution is formed from the nonthermal electrons, with an electronic temperature above that of the lattice. b) Kinetic trace of normalized differential absorbance for Ag nanocubes on an 8 nm Al_2O_3 spacer compared to a 25 nm Al_2O_3 spacer at the gap resonance (top) and to bare Ag nanocubes on SiO_2 in transmission mode (bottom), which exhibit no ultrafast (≈100 fs) decay of the response, arising from the relaxation of highly energetic nonthermal carriers. c) Cross section of the surface charge (top) and electric field profiles (bottom) at the peaks of the interband (IB) transition and plasmon modes for an electric field oriented in-plane. The field strength scale is up to 20× that of free space for the multipolar (Multi) mode, IB transition, and quadrupolar (Quad) mode and 100× that of free space for the gap mode. d) Left: Electromagnetic field distribution inside the nanostructure (defined as $|E/E_0|$), showing strong plasmonic hot spots at the edges of the nanodisk; right: geometry of the system. e) 2D map of the time evolution of the plasmonic spectral change in 8-nm-thick (left) and 4-nm-thick (right) alumina spacer samples, and (bottom) cuts at 1115 nm (left) and 1300 nm (right) showing the time dynamics of the corresponding data in the above panels after excitation of the plasmon. The time dynamics in the 4-nm-thick spacer are drastically different to the thicker spacer, with a new ultrafast component following the excitation near its resonance at 950 nm. (a–c) Reproduced with permission.[158] Copyright 2017, Springer Nature. (d,e) Reproduced with permission.[157] Copyright 2015, Springer Nature.

the entire visible spectrum.[165] Figure 19f shows the experimental results, compared with equivalent systems without hot spots, which evidence an absorption of at least 80% at wavelengths ranging from 400 to 700 nm.

As mentioned above, thermalization of these highly energetic carriers also happens in a very short timescale, which decreases the likelihood of successful injection into the semiconductor when the carrier is not excited close enough to the metal–semiconductor interface.[162,164,169] Moreover, the direction of the carrier momentum is also important: if, for simplicity, we consider it as a ballistic particle, it is clear that it has to travel toward the metal–semiconductor interface in order to traverse it. Then, in order to maximize the number of harvested hot photocarriers, some of the mentioned planar BMMA designs have sought to increase the interfacial area and decrease the width of the metal layer. Complementing this notion, Knight et al. have discussed the possibility of embedding the metal pattern into the semiconductor, with the goal of capturing a larger proportion of excited carriers by allowing additional regions in the momentum space to traverse to the semiconductor or, in other words, adding additional Schottky barriers at additional directions.[170] This idea allows a broader range of polarizations to be excited for a given metal pattern geometry.

In summary, MMPA designs that rely on the generation of hot carriers can be harnessed to create fast and sensitive photodetectors. To create efficient devices, the two key requirements are to use geometries and materials that provide large generation rates of these highly nonthermal carriers, and to provide means to maximize their extraction from the plasmon-supporting structure into the layers that are used to collect the photocurrents. Although some groups have shown enhanced photodetection ability in Si-BMMPA structure, further study is needed to expand this design to other semiconductor materials. Besides, leveraging SPs and LSPRs of metallic structures in the visible and NIR regions are limited by material fabrication techniques. One item to possibly note is that BMMPAs can have the gap controlled vertically, which has a far greater precision at nanometric scales than laterally patterned coupled nanoparticles. So control over the gap and resulting coupling can be much better in "vertical" gap structures like BMMPAs. The dimensions of the structure range from ≈50 to 250 nm, sizes which inevitably involve complicated and expensive FIB or EBL manufacturing processes. In general, the requirements for BMMPA-based photodetection are: high responsivity, simple fabrication with CMOS compatibility, high photoresponsivity, polarization-independence, zero-bias operation, low power consumption, and broadband detection.

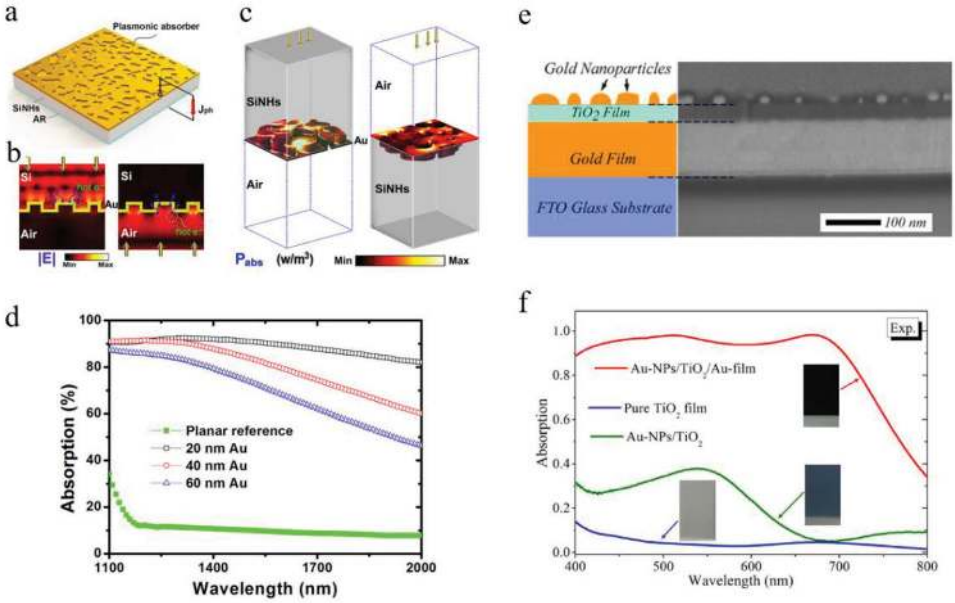

Figure 19. a) Schematic of the proposed plasmonic hot electron photodetector. b,c) Field and volumetric power absorption (P_{abs}) distributions of the device operating at the front and back-illumination modes, from simulations replicating a typical morphology of Au/SiNHs from the experiments. d) Measured absorption spectra under back illumination of the Au/SiNH devices with different thicknesses of Au coatings. The result of a planar reference device with 20 nm thick Au deposited on nonstructured sample is also included. e) Left: Schematic of the metal–dielectric–metal nanostructure that is composed of (from bottom to the top) a FTO glass substrate coated with an optically thick Au film (≈150 nm) followed by a thin TiO_2 film acting as the spacer layer and at the very top, a monolayer of Au NPs with random size dispersion and spatial distribution. Right: Side-view SEM image of the optimized Au-NPs/TiO_2/Au-film nanostructure prepared with a 5-nm-thick Au film predeposited on a 50-nm-thick TiO_2 spacer layer. f) Experimentally measured absorption spectra of the Au-NPs/TiO_2/Au-film nanostructure, the pure TiO_2 film, and the Au-NPs/TiO_2 nanostructure. The insets show the photographic images of the prepared samples. (a–d) Reproduced with permission.[168] Copyright 2017, American Chemical Society. (e,f) Reproduced with permission.[165] Copyright 2016, Springer Nature.

3.3. Bolometers Based on BMMPAs

To suppress dark noise, bulky cryogenic systems are required in infrared photodetectors. Thermal detectors provide portable, low-cost alternatives for IR detection or imaging at room temperature. A bolometer is a device for detecting the power of incident EM radiation via heating of a material with a temperature-dependent electrical resistance, as illustrated in **Figure 20**a. Conventional bolometer design uses thick metal, semiconductor, or superconductor as absorber to guarantee high absorption while BMMPA-based bolometer can boost its performance and decrease thickness significantly.[8,171–175]

Maier and Brückl presented an alternative integrated solution of wavelength-tunable absorption control in thermal microbolometers.[8] Later, a proof-of-concept MMPA-based bolometer was demonstrated in 2012, operating at around 1.5 μm and exhibiting room-temperature time constants of about 134 μs.[175] On this basis, the authors envisioned an integrated bolometer array architecture that would allow for integrated broadband spectroscopy and polarimetry without the need of any external dispersive element or polarizer. Some groups have integrated the BMMPA-based bolometer in compact photoelectric devices.[172,173] A monolithic resonant terahertz sensor element comprising a BMMPA and a microbolometer was reported in 2013, with a minimum noise-equivalent power (NEP) of 37 pW $\sqrt{\text{Hz}}^{-1}$ and a thermal time constant of 68 ms.[172] Ma et al. reported a microbolometer integrated with a BMMPA, superior to an ordinary SiN_x absorber within a broad spectral range, as shown in Figure 20b–e.[173] The MM structure yields three vaguely distinguishable peaks at 7.31, 8.43, and 9.03 μm corresponding to the resonant absorption of their square resonators with a size of 1.5, 2, and 2.5 μm, respectively. The peak originating from the 3 μm size resonator is swallowed by the adjacent peak, but it can be distinguished by the field distribution, as shown in Figure 20e. The *I*–*V* curve in Figure 20f indicates a temperature sensitivity of –8 mV K^{-1}, meaning that the junction voltage will drop by 8 mV as the device temperature rises by 1 K. The responsivity of the bolometer is characterized by the transient response of the device upon IR illumination, as shown in Figure 20g. The BMMPA shows a boost in the responsivity of the microbolometers by as high as 60% under all bias conditions investigated.

Hot electrons are not only promising for photodetection but also present a solution to achieve improved responsivity and NEP. Two different types of phonon-cooled hot-electron bolometers (HEB) are compared: a conventional antenna coupled HEB (AC-HEB) and a novel frequency selective bolometer with a BMMPA.[174] While the optical responsivity and NEP are ≈6 A W^{-1} and ≈20 pW $\sqrt{\text{Hz}}^{-1}$ for the AC-HEB, that of the BMMPA-HEBs is ≈40 A W^{-1} and ≈5 pW $\sqrt{\text{Hz}}^{-1}$, respectively.

Overall, part of the initial motivation to develop BMMPAs is their application in thermal detection, although integrated devices are rarely reported. Although BMMPA-based IR thermal detection demonstrates high responsivity and outperforms

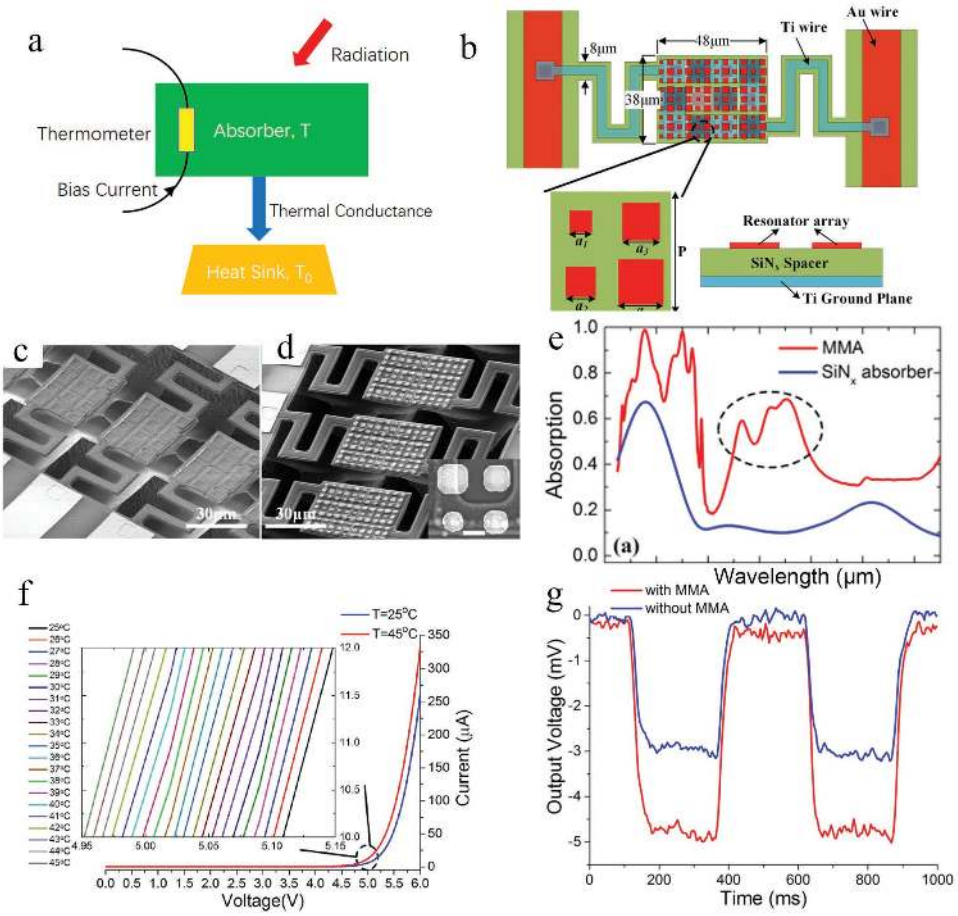

Figure 20. a) A typical bolometer structure including a BMMPA. b) Top view of the designed microbolometer. c,d) SEM pictures of the fabricated microbolometers without and with BMMPA. The zoomed-in picture in (d) is the unit cell of the resonator array (scale bar: 2 μm). e) Simulated absorption of BMMPA and the ordinary SiN_x absorber; f) *I–V* characteristics of the fabricated microbolometer at the two different device temperatures of 25 and 45 °C, respectively. The inset is the zoomed-in view of different *I–V* curves with a 1 °C step around a 10 μA bias. g) Transient responses of the microbolometers under modulated IR incidence at a bias current of 10 μA. (b–g) Reproduced with permission.[173] Copyright 2016, Optical Society of America.

common detection technology without requiring heavy refrigeration systems, a challenge remains in how to bridge the gap between the BMMPA-based bolometer and mainstream CMOS technology. Further investigation needs to focus on solving the compatibility of the BMMPA-based bolometer with integrated circuit fabrication processes.

3.4. MMPAs for Broadband Manipulation of Mechanical Resonances

Stretching forces are commonly utilized to engineer MMPAs. For example, conductive rubber is used as a back layer for dielectric resonators. Due to the different coupling mechanism of rubber, the operation frequency of MMPA blueshifts with increasing strain parallel to the H field but becomes independent on strain variation parallel to the E field.[176] Resonant light in the MM structure can also be efficiently converted into heat based on thermomechanically coupled optical and mechanical resonances or controlling mechanical damping with light.[18,177] BMMPA-based mechanical resonances have several benefits: very low oscillation threshold pump power, parametric mechanical oscillation over an extremely broad frequency range of optical pump frequencies (e.g., ≈4 THz in ref. [18]), low *Q*-factor, and does not strictly require Fano resonances.

In order to mimic real materials and support simultaneous optical and mechanical resonances, Cubukcu and co-workers demonstrated in a pioneering work that the optical and mechanical degrees of freedom of MMs can interact via heating by optical absorption, meaning that one can manipulate the mechanical damping by using light.[18] The structure shown in **Figure 21**a,b is composed of a bilayer gold-SiN membrane containing an array of polarization-independent cross-shaped plasmonic nanoslots and a metal backreflector. When illuminated near its resonance with a continuous-wave 1550 nm laser beam, the optical power is efficiently absorbed and converted into heat on the bilayer membrane. As shown in Figure 21c, the heated membrane deflection results from the plasmomechanical coupling when the structure is illuminated with a pump laser at ω_L corresponding to 1550 nm wavelength, tuned slightly to

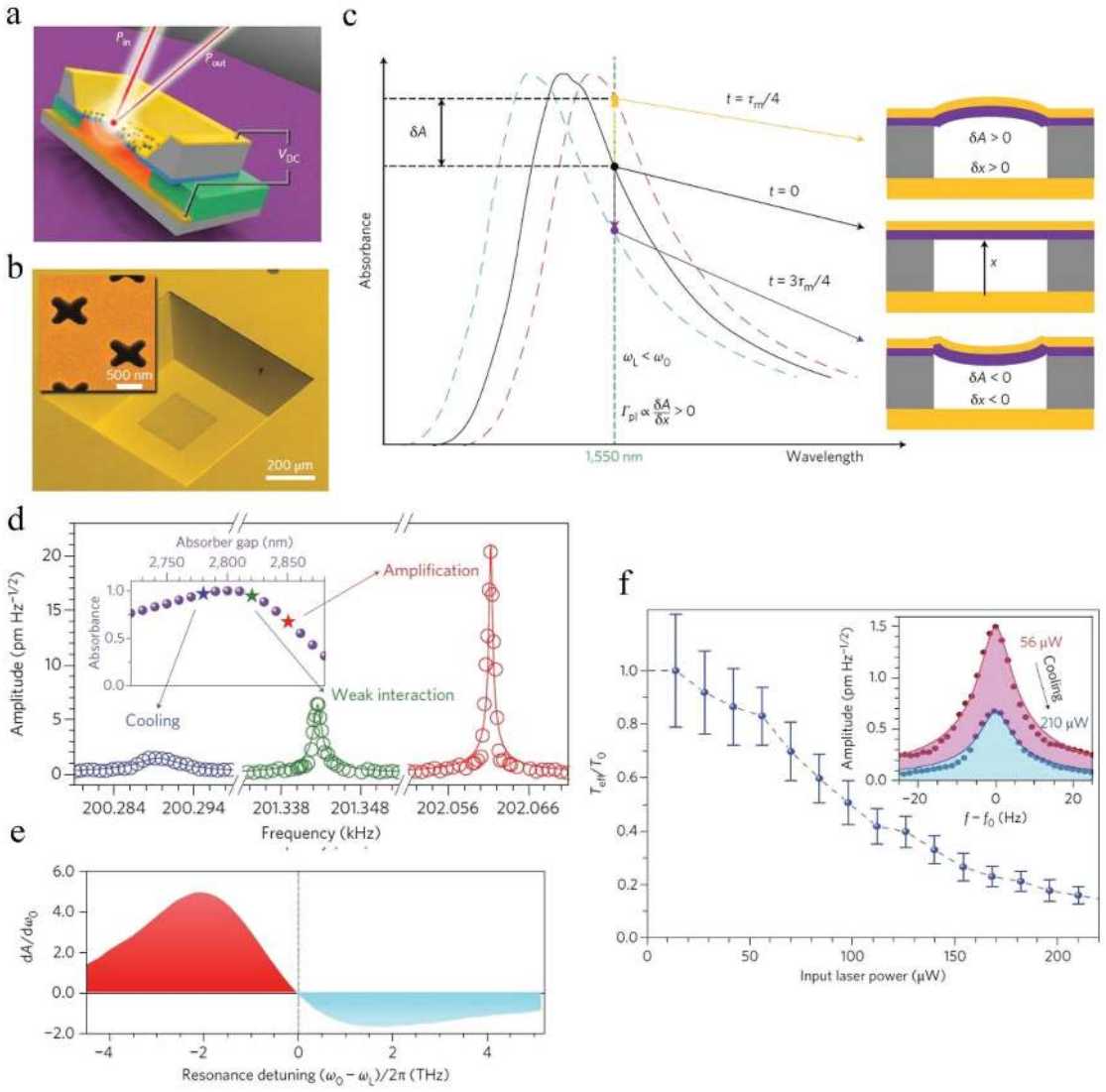

Figure 21. a) Schematic of a MMPA with a mechanically compliant bilayer (Au (25 nm)/SiN (100 nm)) membrane component decorated with a nano-antenna array. b) The false-color SEM image of the fabricated cross-shaped nanoslot (length (360 nm)/width (150 nm)) antenna array (period 800 nm) that covers an area of 250 μm × 250 μm at the center of the 500 μm × 500 μm membrane. Inset: close-up SEM of the array. c) Plasmomechanical coupling: when the MM is illuminated with a pump laser at ω_L corresponding to a wavelength of 1550 nm, tuned slightly to the red side of the Fano resonance frequency ω_0, the natural oscillation of the membrane of amplitude δx at its mechanical resonance frequency ($1/\tau_m$) leads to a dynamic modulation of total absorbance (δA). As δA varies between positive and negative values, this leads to a dynamic modulation on the thermal expansion of the membrane. As illustrated here for positive resonance detuning, that is, $\omega_L < \omega_0$, the light-induced mechanical damping $\Gamma_{pl} \propto \delta A/\delta x$ is always positive, which dampens the mechanical resonance. d) The thermomechanical Brownian noise spectra for the fundamental mechanical resonance measured at a pump power of ≈17 μW for different absorber gap values corresponding to weak (unperturbed), positive (amplification), and negative (cooling) absorption-induced forces. The inset shows the MM absorbance as a function of absorber gap at 1550 nm pump wavelength near the Fano resonance. e) Differential spectral absorbance ($dA/d\omega_0$) versus the detuning between the Fano resonance frequency (ω_0) and the fixed 1550 nm pump laser frequency (ω_L). f) The effective temperature T_{eff} of the fundamental mechanical mode is proportional to the area under its peak thermomechanical noise spectrum, exemplified in the inset. The absorber gap has been tuned at 5.5 V, corresponding to the maximum $|dA/d\omega_0|$ on the red side of the Fano resonance. At 210 μW pump power, T_{eff} for the Brownian motion of the mechanical mode is reduced below 50 K from room temperature (T_0 = 300 K). (a–f) Reproduced with permission.[18] Copyright 2016, Springer Nature.

the red side of the Fano resonance frequency ω_0. The absorbance will be tuned by δA due to changes in the absorber gap originating from the natural oscillation of the membrane with amplitude δx at its mechanical resonance frequency ($1/\tau_m$), where τ_m is the period of the mechanical oscillation. The light-induced damping $\Gamma_{pl} \propto \delta A/\delta x$ is able to increase or decrease the initial mechanical damping depending on its sign as shown in Figure 21d. For positive resonance detuning, that is, $\omega_L < \omega_0$, Γ_{pl} is always positive, which dampens the mechanical resonance, whereas for $\omega_L > \omega_0$, mechanical amplification, that is, gain, is possible since Γ_{pl} is always negative, as shown in Figure 21e. As a result, solely by optical pumping at 210 μW, the effective

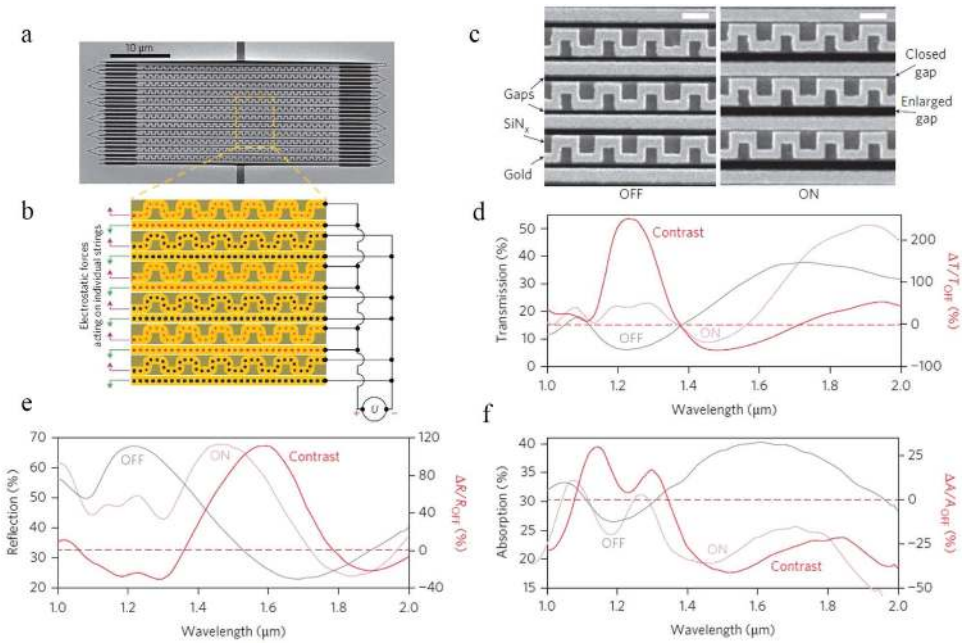

Figure 22. a) SEM image of the electrically reconfigurable device. b) Schematic of the driving circuit (black) and a section of the MM pattern consisting of a gold nanostructure (yellow) supported by silicon nitride strings (brown). The driving voltage *U* causes positive (red) and negative (blue) charging and thus electrostatic forces acting in opposite directions (pink and green). c) SEM images of the MM in its OFF and ON states. Scale bar: 500 nm. d) Transmission, e) reflection, and f) absorption spectra of the device in the OFF and ON states (left axis) and the corresponding switching contrast (right axis). Reproduced with permission.[87] Copyright 2013, Springer Nature.

temperature of the mechanical mode can be reduced down to 48 K from room temperature, as shown in Figure 21f.

In addition to showing manipulation of mechanical damping by light, the BMMPA demonstrates its utility on electromechanical applications. Electromechanical BMMPAs have been demonstrated operating under sub-terahertz,[178] terahertz,[179] and near-infrared spectra.[87] After introducing the BMMPA structure, their modulation speed can be increased by several orders of magnitude, and is thus promising for further applications in tunable spectral filters, switches, modulators, adaptable transformation optics devices, etc. Zheludev and coworkers proposed an approach based on combining the elastic properties of a nanoscale-thickness dielectric membrane with nanoscale electrostatic forces in a planar BMMPA, providing a powerful generic platform for achieving tunable MM characteristics in the optical spectral range.[87] The colossal electro-optical response of MMs guarantees either fast continuous tuning of its optical properties or high-contrast irreversible switching in a device only 100 nm thick, without external polarizers and analyzers. The electrically reconfigurable photonic MM and a schematic of the driving circuit and a section of the MM pattern consisting of a gold nanostructure supported by SiN strings are shown in **Figure 22**a,b. The reversible electro-optical tuning and modulation spectra indicate that the transmittance may be modulated by ≈5% around 1.1 and 1.3 μm while the reflectance can be modulated by up to 8% around 1.5 μm.[87] As MHz bandwidth electro-optical modulators, the mechanical systems can be easily driven to frequencies up to their fundamental resonance. The power consumption is determined numerically to be small (≈100 fJ). The material's high-contrast, nonvolatile electro-optical switch properties are evaluated by ON and OFF states and the corresponding contrast, as shown in Figure 22c. The transmission, reflection, and absorption (*T*, *R*, and *A*) of the MM redshift by 20% when the device switches, leading to a dramatic change of 250% in *T* around 1.2 mm and a change of 110% in *R* around 1.6 mm, as shown in Figure 22d–f, respectively. Therefore, the BMMPA allows fast continuous tuning of its optical properties and high-contrast irreversible switching in a device of only 100 nm thick, without external polarizers and analyzers.

Although it is an easy task to find the solution for electromechanical/thermomechanical manipulation within the THz or sub-THz region, devices working in the visible and near-infrared range are challenging because of the required nanoscale fabrication. The electromechanical manipulation provides an opportunity to achieve tunable spectral filters, switches, modulators, protective optical circuitry, optical networks, and adaptable transformation optical devices. Thermomechanical coupling facilitates optical manipulation of the dynamics of mechanical oscillators and provides a mean to introduce effective cooling. By using the two mechanisms, further work should be focused on experimental demonstration of these devices.

4. Outlook and Comments

In the past decade, a wide variety of BMMPAs covering wide spectral regimes have been experimentally and theoretically demonstrated due to the significant advances in device fabrication and theoretical modeling. This review summarizes versatile methods with facile design and geometrical scalability, highlighting the

ideas behind BMMPAs working at different frequencies, as well as providing guidance on how to optimize design parameters to fulfil diverse application requirements. Most of the BMMPAs are polarization-insensitive due to the symmetric patterns on the top and maintain high absorption over a large range of incidence angle. However, the field of BMMPA research is still at its infancy. Formidable technological challenges remain, as some theoretically demonstrated ideas are too sophisticated to fabricate, limited by the present fabrication technology, for example, BMMPAs based on 2D materials. These require atomic thickness processing and nanoscale patterning resolution and thus inevitably involve multistep fabrication and costly FIB or EBL techniques. Furthermore, more effort is required to bridge the gap between the high yield in large fabricated areas and low cost. Solar energy harvesting devices, for instance, are of great significance to address the energy crisis worldwide. BMMPAs provide a great potential to achieve high-efficiency PV devices with theoretical prediction of STPV systems of up to 85% efficiency and ultrathin solar cells. Devices operating from visible to NIR regions of the spectrum need nanosized resonators in BMMPA designs because the absorption frequencies critically rely on the size of the resonators. However, present fabrication methods of resonators depend mainly on expensive fabrication methods, which are ill-suited for large-scale production. Self-assembly and casting-based techniques are promising for fabricating cost-effective PV devices based on BMMPAs. Finally, two "smalls" must be taken into account: to obtain small device sizes at low frequency and to conquer small effects at the nanoscale. On the one hand, since the lattice parameter increases for BMMPA operating at lower frequency, narrowing down the size of resonator at low frequency is desired for compact integrated circuits and industrial communication devices. On the other hand, when resonators have nanoscale size, their physical properties are different, such as melting point, oxidation, and grain boundary effects, leading to a complicated design.

In addition to the applications reviewed in this paper, we should bear in mind that we can design BMMPAs for other applications as long as we converted the absorbed light into something useful, for example, into an electrical signal. Overall, although faced with formidable challenges to overcome, the rapidly expanding BMMPA research give us the confidence that their tunable, versatile applications will renew absorption-based devices and they will be adopted by the industry in the near future.

Acknowledgements

This work was supported by National Basic Research Program of China (Project No. 2013CB933301) and National Natural Science Foundation of China (Project No. 51272038). L.V.B. was supported by China Postdoctoral Science Foundation. A.O.G. was supported by the Volkswagen Foundation (Germany) and via the Chang Jiang (Yangtze River) Chair Professorship (China). G.P.W. acknowledges support from the Center for Nanoscale Materials, a U.S. Department of Energy Office of Science User Facility, and support by the U.S. Department of Energy, Office of Science, under Contract No. DE-AC02-06CH11357. In addition, the authors acknowledge financial support obtained from the Virtual Institute for Theoretical Photonics and Energy. This review is part of the *Advanced Optical Materials* Hall of Fame article series, which recognizes the excellent contributions of leading researchers to the field of optical materials science.

Conflict of Interest

The authors declare no conflict of interest.

Keywords

absorbers, broadband, metamaterials, metasurfaces

Received: July 29, 2018
Published online: October 4, 2018

[1] D. R. Smith, W. J. Padilla, D. Vier, S. C. Nemat-Nasser, S. Schultz, *Phys. Rev. Lett.* **2000**, *84*, 4184.
[2] H. Chen, B.-I. Wu, B. Zhang, J. A. Kong, *Phys. Rev. Lett.* **2007**, *99*, 063903.
[3] N. Seddon, T. Bearpark, *Science* **2003**, *302*, 1537.
[4] D. Smith, S. Schultz, P. Markoš, C. Soukoulis, *Phys. Rev. B* **2002**, *65*, 195104.
[5] N. I. Landy, S. Sajuyigbe, J. Mock, D. Smith, W. Padilla, *Phys. Rev. Lett.* **2008**, *100*, 207402.
[6] J. Hao, J. Wang, X. Liu, W. J. Padilla, L. Zhou, M. Qiu, *Appl. Phys. Lett.* **2010**, *96*, 251104.
[7] C. M. Watts, X. Liu, W. J. Padilla, *Adv. Mater.* **2012**, *24*, OP98.
[8] T. Maier, H. Brückl, *Opt. Lett.* **2009**, *34*, 3012.
[9] X. Liu, T. Starr, A. F. Starr, W. J. Padilla, *Phys. Rev. Lett.* **2010**, *104*, 207403.
[10] N. Liu, M. Mesch, T. Weiss, M. Hentschel, H. Giessen, *Nano Lett.* **2010**, *10*, 2342.
[11] M. K. Hedayati, M. Javaherirahim, B. Mozooni, R. Abdelaziz, A. Tavassolizadeh, V. S. K. Chakravadhanula, V. Zaporojtchenko, T. Strunkus, F. Faupel, M. Elbahri, *Adv. Mater.* **2011**, *23*, 5410.
[12] C. Wu, B. Neuner III, J. John, A. Milder, B. Zollars, S. Savoy, G. Shvets, *J. Opt.* **2012**, *14*, 024005.
[13] H.-T. Chen, *Opt. Express* **2012**, *20*, 7165.
[14] R. Alaee, M. Farhat, C. Rockstuhl, F. Lederer, *Opt. Express* **2012**, *20*, 28017.
[15] D. Shrekenhamer, W.-C. Chen, W. J. Padilla, *Phys. Rev. Lett.* **2013**, *110*, 177403.
[16] W. Li, U. Guler, N. Kinsey, G. V. Naik, A. Boltasseva, J. Guan, V. M. Shalaev, A. V. Kildishev, *Adv. Mater.* **2014**, *26*, 7959.
[17] a) A. Tittl, A. K. U. Michel, M. Schäferling, X. Yin, B. Gholipour, L. Cui, M. Wuttig, T. Taubner, F. Neubrech, H. Giessen, *Adv. Mater.* **2015**, *27*, 4597; b) X. Liu, W. J. Padilla, *Optica* **2017**, *4*, 430.
[18] H. Zhu, F. Yi, E. Cubukcu, *Nat. Photonics* **2016**, *10*, 709.
[19] a) C. Kurter, J. Abrahams, S. M. Anlage, *Appl. Phys. Lett.* **2010**, *96*, 253504; b) B. Edwards, A. Alù, M. E. Young, M. Silveirinha, N. Engheta, *Phys. Rev. Lett.* **2008**, *100*, 033903; c) G. Scalari, C. Maissen, D. Turčinková, D. Hagenmüller, S. De Liberato, C. Ciuti, C. Reichl, D. Schuh, W. Wegscheider, M. Beck, *Science* **2012**, *335*, 1323; d) I. Zolotovskii, D. Korobko, R. Minvaliev, V. Ostatochnikov, *Opt. Spectrosc.* **2014**, *117*, 822; e) I. Sersic, M. Frimmer, E. Verhagen, A. F. Koenderink, *Phys. Rev. Lett.* **2009**, *103*, 213902; f) A. Christ, O. J. Martin, Y. Ekinci, N. A. Gippius, S. G. Tikhodeev, *Nano Lett.* **2008**, *8*, 2171.
[20] A. G. Paulish, P. S. Zagubisalo, S. A. Kuznetsov, presented at 38th Int. Conf. Infrared, Millimeter, and Terahertz Waves (IRMMW-THz), Mainz, Germany, September **2013**.
[21] Z. H. Jiang, S. Yun, F. Toor, D. H. Werner, T. S. Mayer, *ACS Nano* **2011**, *5*, 4641.
[22] P. Yu, J. Wu, E. Ashalley, A. Govorov, Z. Wang, *J. Phys. D: Appl. Phys.* **2016**, *49*, 365101.

[23] L. Luo, I. Chatzakis, J. Wang, F. B. Niesler, M. Wegener, T. Koschny, C. M. Soukoulis, *Nat. Commun.* **2014**, *5*, 3055.
[24] K. Aydin, V. E. Ferry, R. M. Briggs, H. A. Atwater, *Nat. Commun.* **2011**, *2*, 517.
[25] B. Reinhard, K. M. Schmitt, V. Wollrab, J. Neu, R. Beigang, M. Rahm, *Appl. Phys. Lett.* **2012**, *100*, 221101.
[26] Z. Yong, S. Zhang, C. Gong, S. He, *Sci. Rep.* **2016**, *6*, 24063.
[27] a) X. Liu, T. Tyler, T. Starr, A. F. Starr, N. M. Jokerst, W. J. Padilla, *Phys. Rev. Lett.* **2011**, *107*, 045901; b) P. Bermel, M. Ghebrebrhan, M. Harradon, Y. X. Yeng, I. Celanovic, J. D. Joannopoulos, M. Soljacic, *Nanoscale Res. Lett.* **2011**, *6*, 549.
[28] D. Shrekenhamer, W. Xu, S. Venkatesh, D. Schurig, S. Sonkusale, W. J. Padilla, *Phys. Rev. Lett.* **2012**, *109*, 177401.
[29] K. Chen, R. Adato, H. Altug, *ACS Nano* **2012**, *6*, 7998.
[30] K.-T. Lin, H.-L. Chen, Y.-S. Lai, C.-C. Yu, *Nat. Commun.* **2014**, *5*, 3288.
[31] B. Casse, W. Lu, Y. Huang, E. Gultepe, L. Menon, S. Sridhar, *Appl. Phys. Lett.* **2010**, *96*, 023114.
[32] M. Gil, J. Bonache, F. Martin, *Metamaterials* **2008**, *2*, 186.
[33] M. D. Astorino, F. Frezza, N. Tedeschi, presented at 2016 URSI Int. Symp. Electromagnetic Theory (EMTS), Espoo, Finland, August **2016**.
[34] Y. Lee, P. Tuong, H. Zheng, J. Rhee, W. Jang, *J. Korean Phys. Soc.* **2012**, *60*, 1203.
[35] P. Yu, L. V. Besteiro, J. Wu, Y. Huang, Y. Wang, A. O. Govorov, Z. Wang, *Opt. Express* **2018**, *26*, 20471.
[36] P. Pitchappa, C. P. Ho, P. Kropelnicki, N. Singh, D.-L. Kwong, C. Lee, *J. Appl. Phys.* **2014**, *115*, 193109.
[37] Y. J. Yoo, Y. J. Kim, P. Van Tuong, J. Y. Rhee, K. W. Kim, W. H. Jang, Y. Kim, H. Cheong, Y. Lee, *Opt. Express* **2013**, *21*, 32484.
[38] S. Bhattacharyya, S. Ghosh, K. V. Srivastava, *J. Appl. Phys.* **2013**, *114*, 094514.
[39] L. Huang, H. Chen, *Prog. Electromagn. Res.* **2011**, *113*, 103.
[40] G. Dayal, S. A. Ramakrishna, *J. Opt.* **2013**, *15*, 055106.
[41] Y. Q. Ye, Y. Jin, S. He, *J. Opt. Soc. Am. B* **2010**, *27*, 498.
[42] S. Gu, J. Barrett, T. Hand, B.-I. Popa, S. Cummer, *J. Appl. Phys.* **2010**, *108*, 064913.
[43] G. Chao, Q. Shao-Bo, P. Zhi-Bin, Z. Hang, X. Zhuo, B. Peng, P. Wei-Dong, L. Bao-Qin, *Chin. Phys. Lett.* **2010**, *27*, 117802.
[44] J. Chen, X. Huang, G. Zerihun, Z. Hu, S. Wang, G. Wang, X. Hu, M. Liu, *J. Electron. Mater.* **2015**, *44*, 4269.
[45] Y. Z. Cheng, Y. Wang, Y. Nie, R. Z. Gong, X. Xiong, X. Wang, *J. Appl. Phys.* **2012**, *111*, 044902.
[46] J. Rhee, Y. Yoo, K. Kim, Y. Kim, Y. Lee, *J. Electromagn. Waves Appl.* **2014**, *28*, 1541.
[47] a) M. K. Hedayati, F. Faupel, M. Elbahri, *Materials* **2014**, *7*, 1221; b) S. Ogawa, M. Kimata, *Materials* **2018**, *11*, 458; c) L. Huang, H. T. Chen, *Terahertz Sci. Technol.* **2013**, *6*, 26.
[48] X. Zhao, K. Song, *AIP Adv.* **2014**, *4*, 100701.
[49] a) Y. Wu, J. Li, Z.-Q. Zhang, C. Chan, *Phys. Rev. B* **2006**, *74*, 085111; b) B. A. Slovick, Z. G. Yu, S. Krishnamurthy, *Phys. Rev. B* **2014**, *89*, 155118.
[50] J. Zhou, L. Zhang, G. Tuttle, T. Koschny, C. M. Soukoulis, *Phys. Rev. B* **2006**, *73*, 041101.
[51] G. Duan, J. Schalch, X. Zhao, J. Zhang, R. D. Averitt, X. Zhang, *Phys. Rev. B* **2018**, *97*, 035128.
[52] A. Rasoul, A. Mohammad, R. Carsten, *J. Phys. D: Appl. Phys.* **2017**, *50*, 503002.
[53] a) P. Rufangura, C. Sabah, *Vacuum* **2015**, *120*, 68; b) B. Mulla, C. Sabah, *Waves Random Complex Media* **2015**, *25*, 382.
[54] H. Li, L. H. Yuan, B. Zhou, X. P. Shen, Q. Cheng, T. J. Cui, *J. Appl. Phys.* **2011**, *110*, 014909.
[55] M. Navarro-Cía, M. Beruete, I. Campillo, M. Sorolla, *Phys. Rev. B* **2011**, *83*, 115112.
[56] H.-T. Hsu, C.-J. Wu, *Prog. Electromagn. Res. Lett.* **2009**, *9*, 101.
[57] a) Y. Huang, Y. Tian, G. Wen, W. Zhu, *J. Opt.* **2013**, *15*, 055104; b) Y.-J. Huang, G.-J. Wen, J. Li, W.-R. Zhu, P. Wang, Y.-H. Sun, *J. Electromagn. Waves Appl.* **2013**, *27*, 552.
[58] S. Gu, B. Su, X. Zhao, *J. Appl. Phys.* **2013**, *114*, 163702.
[59] B. Shi, L. Chun-Rong, Z. Yan-Ping, Z. Xiao-Peng, *Acta Phys. Sin.* **2010**, *5*, 42.
[60] P. Tuong, J. Park, J. Rhee, K. Kim, H. Cheong, W. Jang, Y. Lee, *Mater. Chem. Phys.* **2013**, *141*, 535.
[61] W. Zhu, X. Zhao, B. Gong, L. Liu, B. Su, *Appl. Phys. A* **2011**, *102*, 147.
[62] W. Ma, Y. Wen, X. Yu, *Opt. Express* **2013**, *21*, 30724.
[63] L. Huang, D. R. Chowdhury, S. Ramani, M. T. Reiten, S.-N. Luo, A. J. Taylor, H.-T. Chen, *Opt. Lett.* **2012**, *37*, 154.
[64] Y. Cheng, Y. Nie, R. Gong, *Opt. Laser Technol.* **2013**, *48*, 415.
[65] M. Soheilifar, R. Sadeghzadeh, *AEU - Int. J. Electron. Commun.* **2015**, *69*, 126.
[66] M. Choi, S. H. Lee, Y. Kim, S. B. Kang, J. Shin, M. H. Kwak, K.-Y. Kang, Y.-H. Lee, N. Park, B. Min, *Nature* **2011**, *470*, 369.
[67] H. Wang, L. Wang, *Opt. Express* **2013**, *21*, A1078.
[68] H. Wang, V. P. Sivan, A. Mitchell, G. Rosengarten, P. Phelan, L. Wang, *Sol. Energy Mater. Sol. Cells* **2015**, *137*, 235.
[69] J. A. Bossard, L. Lin, S. Yun, L. Liu, D. H. Werner, T. S. Mayer, *ACS Nano* **2014**, *8*, 1517.
[70] J. Zhu, Z. Ma, W. Sun, F. Ding, Q. He, L. Zhou, Y. Ma, *Appl. Phys. Lett.* **2014**, *105*, 021102.
[71] D. Hu, H. Wang, Z. Tang, X. Zhang, *Appl. Opt.* **2016**, *55*, 5257.
[72] S. Molesky, C. J. Dewalt, Z. Jacob, *Opt. Express* **2013**, *21*, A96.
[73] C. Zhang, Q. Cheng, J. Yang, J. Zhao, T. J. Cui, *Appl. Phys. Lett.* **2017**, *110*, 143511.
[74] G. Deng, J. Yang, Z. Yin, *Appl. Opt.* **2017**, *56*, 2449.
[75] Y. Zhang, Y. Li, Y. Cao, Y. Liu, H. Zhang, *Opt. Commun.* **2017**, *382*, 281.
[76] B. Vasić, R. Gajić, *Appl. Phys. Lett.* **2013**, *103*, 261111.
[77] Z. Su, J. Yin, X. Zhao, *Opt. Express* **2015**, *23*, 1679.
[78] S. He, T. Chen, *IEEE Trans. Terahertz Sci. Technol.* **2013**, *3*, 757.
[79] J. Wang, Y. Jiang, *Opt. Express* **2017**, *25*, 5206.
[80] M. K. Hedayati, F. Faupel, M. Elbahri, *Appl. Phys. A* **2012**, *109*, 769.
[81] K. Chaudhuri, M. Alhabeb, Z. Wang, V. M. Shalaev, Y. Gogotsi, A. Boltasseva, *ACS Photonics* **2018**, *5*, 1115.
[82] Y. Cui, K. H. Fung, J. Xu, H. Ma, Y. Jin, S. He, N. X. Fang, *Nano Lett.* **2012**, *12*, 1443.
[83] Y. Bai, L. Zhao, D. Ju, Y. Jiang, L. Liu, *Opt. Express* **2015**, *23*, 8670.
[84] R. Feng, J. Qiu, L. Liu, W. Ding, L. Chen, *Opt. Express* **2014**, *22*, A1713.
[85] B. Zhang, Y. Zhang, J. Duan, W. Zhang, W. Wang, *Sensors* **2016**, *16*, 1153.
[86] G.-H. Yang, X.-X. Liu, Y.-L. Lv, J.-H. Fu, Q. Wu, X. Gu, *J. Appl. Phys.* **2014**, *115*, 17E523.
[87] J.-Y. Ou, E. Plum, J. Zhang, N. I. Zheludev, *Nat. Nanotechnol.* **2013**, *8*, 252.
[88] F. Dincer, O. Akgol, M. Karaaslan, E. Unal, C. Sabah, *Prog. Electromagn. Res.* **2014**, *144*, 93.
[89] Y. Pang, J. Wang, Q. Cheng, S. Xia, X. Y. Zhou, Z. Xu, T. J. Cui, S. Qu, *Appl. Phys. Lett.* **2017**, *110*, 104103.
[90] H. Xiong, J.-S. Hong, C.-M. Luo, L.-L. Zhong, *J. Appl. Phys.* **2013**, *114*, 064109.
[91] Y. Liu, S. Gu, C. Luo, X. Zhao, *Appl. Phys. A* **2012**, *108*, 19.
[92] X. Zhao, K. Fan, J. Zhang, H. R. Seren, G. D. Metcalfe, M. Wraback, R. D. Averitt, X. Zhang, *Sens. Actuators A* **2015**, *231*, 74.
[93] J. Grant, Y. Ma, S. Saha, A. Khalid, D. R. Cumming, *Opt. Lett.* **2011**, *36*, 3476.
[94] Y. Z. Cheng, W. Withayachumnankul, A. Upadhyay, D. Headland, Y. Nie, R. Z. Gong, M. Bhaskaran, S. Sriram, D. Abbott, *Appl. Phys. Lett.* **2014**, *105*, 181111.
[95] C. Wu, G. Shvets, *Opt. Lett.* **2012**, *37*, 308.

[96] C. Hu, L. Liu, Z. Zhao, X. N. Chen, X. Luo, *Opt. Express* **2009**, *17*, 16745.
[97] R. R. Nair, P. Blake, A. N. Grigorenko, K. S. Novoselov, T. J. Booth, T. Stauber, N. M. Peres, A. K. Geim, *Science* **2008**, *320*, 1308.
[98] S. H. Lee, M. Choi, T.-T. Kim, S. Lee, M. Liu, X. Yin, H. K. Choi, S. S. Lee, C.-G. Choi, S.-Y. Choi, *Nat. Mater.* **2012**, *11*, 936.
[99] D.-E. Wen, H. Yang, Q. Ye, M. Li, L. Guo, J. Zhang, *Phys. Scr.* **2013**, *88*, 015402.
[100] Q. Liang, T. Wang, Z. Lu, Q. Sun, Y. Fu, W. Yu, *Adv. Opt. Mater.* **2013**, *1*, 43.
[101] a) J. Sun, L. Liu, G. Dong, J. Zhou, *Opt. Express* **2011**, *19*, 21155; b) J. Yang, X. Hu, X. Li, Z. Liu, Z. Liang, X. Jiang, J. Zi, *Phys. Rev. B* **2009**, *80*, 125103; c) H.-T. Chen, J. Zhou, J. F. O'Hara, F. Chen, A. K. Azad, A. J. Taylor, *Phys. Rev. Lett.* **2010**, *105*, 073901.
[102] F. Ding, Y. Cui, X. Ge, Y. Jin, S. He, *Appl. Phys. Lett.* **2012**, *100*, 103506.
[103] B.-X. Wang, L.-L. Wang, G.-Z. Wang, W.-Q. Huang, X.-F. Li, X. Zhai, *IEEE Photonics Technol. Lett.* **2014**, *26*, 111.
[104] S. Agarwal, Y. Prajapati, *Appl. Phys. A* **2016**, *122*, 561.
[105] M. Amin, M. Farhat, H. Bağcı, *Opt. Express* **2013**, *21*, 29938.
[106] X. Jia, X. Wang, C. Yuan, Q. Meng, Z. Zhou, *J. Appl. Phys.* **2016**, *120*, 033101.
[107] X. Zhu, W. Yan, P. U. Jepsen, O. Hansen, N. A. Mortensen, S. Xiao, *Appl. Phys. Lett.* **2013**, *102*, 131101.
[108] G. Konstantatos, M. Badioli, L. Gaudreau, J. Osmond, M. Bernechea, F. P. G. De Arquer, F. Gatti, F. H. Koppens, *Nat. Nanotechnol.* **2012**, *7*, 363.
[109] S. Li, J. Gao, X. Cao, W. Li, Z. Zhang, D. Zhang, *J. Appl. Phys.* **2014**, *116*, 043710.
[110] Y. Shi, Y. C. Li, T. Hao, L. Li, C.-H. Liang, *Waves Random Complex Media* **2017**, *27*, 381.
[111] X. Kong, J. Xu, J.-J. Mo, S. Liu, *Front. Optoelectron.* **2017**, *10*, 124.
[112] D. Lee, H. Jeong, S. Lim, *Sci. Rep.* **2017**, *7*, 4891.
[113] T. T. Nguyen, S. Lim, *Appl. Phys. Lett.* **2018**, *112*, 021605.
[114] J. Wu, P. Yu, A. S. Susha, K. A. Sablon, H. Chen, Z. Zhou, H. Li, H. Ji, X. Niu, A. O. Govorov, A. L. Rogach, Z. M. Wang, *Nano Energy* **2015**, *13*, 827.
[115] a) P. Yu, Y. Yao, J. Wu, X. Niu, A. L. Rogach, Z. Wang, *Sci. Rep.* **2017**, *7*, 7696; b) Y. Peng, Z. Fanlu, L. Ziyuan, Z. Zhiqin, G. Alexander, F. Lan, T. Hoe, J. Chennupati, W. Zhiming, *J. Phys. D: Appl. Phys.* **2018**, *51*, 295106.
[116] M. Hedayati, A. Zillohu, T. Strunskus, F. Faupel, M. Elbahri, *Appl. Phys. Lett.* **2014**, *104*, 041103.
[117] T. Ji, L. Peng, Y. Zhu, F. Yang, Y. Cui, X. Wu, L. Liu, S. He, F. Zhu, Y. Hao, *Appl. Phys. Lett.* **2015**, *106*, 161107.
[118] T. Ji, Y. Wang, Y. Cui, Y. Lin, Y. Hao, D. Li, *Mater. Today Energy* **2017**, *5*, 181.
[119] A. Biswas, H. Eilers, F. Hidden Jr., O. Aktas, C. Kiran, *Appl. Phys. Lett.* **2006**, *88*, 013103.
[120] L. Meiling, M. Badar, Y. Zixuan, Z. Qi, *Adv. Opt. Mater.* **2018**, *6*, 1701238.
[121] N. F. Hadley, *Science* **1979**, *203*, 367.
[122] K. Tanaka, Y. Fujiyama, R. Tomokane, H. Koga, S. Akita, T. Nosaka, Y. Nakayama, M. Tonouchi, in *Joint 32nd Int. Conf. Infrared and Millimeter Waves, 2007 and the 2007 15th Int. Conf. Terahertz Electronics (IRMMW-THz)*, IEEE, Piscataway, NJ **2007**, pp. 346–347.
[123] A. Saib, L. Bednarz, R. Daussin, C. Bailly, X. Lou, J.-M. Thomassin, C. Pagnoulle, C. Detrembleur, R. Jérôme, I. Huynen, *IEEE Trans. Microwave Theory Tech.* **2006**, *54*, 2745.
[124] W. Zhu, Y. Huang, I. D. Rukhlenko, G. Wen, M. Premaratne, *Opt. Express* **2012**, *20*, 6616.
[125] Y. Yong-Jun, H. Yong-Jun, W. Guang-Jun, Z. Jing-Ping, S. Hai-Bin, O. Gordon, *Chin. Phys. B* **2012**, *21*, 038501.
[126] a) L. Liu, H. Peng, Y. Pu, X. Ying, Z. Li, J. Xu, Y. Jiang, Z. Liu, *Opt. Express* **2018**, *26*, 1064; b) S. Butun, K. Aydin, *Opt. Express* **2014**, *22*, 19457.
[127] F. Ding, J. Dai, Y. Chen, J. Zhu, Y. Jin, S. I. Bozhevolnyi, *Sci. Rep.* **2016**, *6*, 39445.
[128] J. R. Hendrickson, S. Vangala, C. Dass, R. Gibson, J. Goldsmith, K. Leedy, D. E. Walker, J. W. Cleary, W. Kim, J. Guo, *ACS Photonics* **2018**, *5*, 776.
[129] A. Noor, Z. Hu, *J. Infrared Millim. Terahertz Waves* **2010**, *31*, 791.
[130] M. Decker, I. Staude, I. I. Shishkin, K. B. Samusev, P. Parkinson, V. K. Sreenivasan, A. Minovich, A. E. Miroshnichenko, A. Zvyagin, C. Jagadish, *Nat. Commun.* **2013**, *4*, 2949.
[131] Y. Shen, J. Zhang, Y. Pang, J. Wang, H. Ma, S. Qu, *Opt. Express* **2018**, *26*, 15665.
[132] a) K. Bi, G. Dong, X. Fu, J. Zhou, *Appl. Phys. Lett.* **2013**, *103*, 131915; b) F. J. Rachford, D. N. Armstead, V. G. Harris, C. Vittoria, *Phys. Rev. Lett.* **2007**, *99*, 057202.
[133] Y. Huang, G. Wen, W. Zhu, J. Li, L.-M. Si, M. Premaratne, *Opt. Express* **2014**, *22*, 16408.
[134] a) C. Hägglund, S. P. Apell, *J. Phys. Chem. Lett.* **2012**, *3*, 1275; b) J. N. Munday, H. A. Atwater, *Nano Lett.* **2011**, *11*, 2195.
[135] A. Rothschild, E. Sharlin, G. Ankonina, H. Dotan, I. Dumchin, M. Gross, O. Kfir, O. Blank, *Nat. Mater.* **2013**, *12*, 158.
[136] N.-P. Harder, P. Würfel, *Semicond. Sci. Technol.* **2003**, *18*, S151.
[137] S. J. Kim, P. Fan, J.-H. Kang, M. L. Brongersma, *Nat. Commun.* **2015**, *6*, 7591.
[138] a) V. Aroutiounian, S. Petrosyan, A. Khachatryan, K. Touryan, *J. Appl. Phys.* **2001**, *89*, 2268; b) P. Yu, J. Wu, L. Gao, H. Liu, Z. Wang, *Sol. Energy Mater. Sol. Cells* **2017**, *161*, 377.
[139] P. Yu, J. Wu, S. Liu, J. Xiong, C. Jagadish, Z. M. Wang, *Nano Today* **2016**, *11*, 704.
[140] a) P. Yu, Y. Yao, J. Wu, X. Niu, A. L. Rogach, Z. Wang, *Sci. Rep.* **2017**, *7*, 7696; b) E. Garnett, P. Yang, *Nano Lett.* **2010**, *10*, 1082.
[141] V. Rinnerbauer, A. Lenert, D. M. Bierman, Y. X. Yeng, W. R. Chan, R. D. Geil, J. J. Senkevich, J. D. Joannopoulos, E. N. Wang, M. Soljačić, *Adv. Energy Mater.* **2014**, *4*, 14000334.
[142] J. B. Chou, Y. X. Yeng, Y. E. Lee, A. Lenert, V. Rinnerbauer, I. Celanovic, M. Soljačić, N. X. Fang, E. N. Wang, S. G. Kim, *Adv. Mater.* **2014**, *26*, 8041.
[143] E. Rephaeli, S. Fan, *Opt. Express* **2009**, *17*, 15145.
[144] Q. Jiang, S. Zhang, M. Zhao, *Mater. Chem. Phys.* **2003**, *82*, 225.
[145] a) V. Andreev, A. Vlasov, V. Khvostikov, O. Khvostikova, P. Gazaryan, S. Sorokina, N. Sadchikov, *J. Sol. Energy Eng.* **2007**, *129*, 298; b) C. Ungaro, S. K. Gray, M. C. Gupta, *Opt. Express* **2015**, *23*, A1149; c) Y. Huang, L. Liu, M. Pu, X. Li, X. Ma, X. Luo, *Nanoscale* **2018**, *10*, 8298.
[146] J. H. Park, S. E. Han, P. Nagpal, D. J. Norris, *ACS Photonics* **2016**, *3*, 494.
[147] A. Kohiyama, M. Shimizu, H. Yugami, *Appl. Phys. Express* **2016**, *9*, 112302.
[148] a) Y. Nam, A. Lenert, Y. X. Yeng, P. Bermel, M. Soljačić, E. N. Wang, in *17th Int. Conf. Solid-State Sensors, Actuators and Microsystems (Transducers & Eurosensors XXVII)*, IEEE, Barcelona, Spain **2013**, pp. 1372–1375; b) A. Lenert, D. M. Bierman, Y. Nam, W. R. Chan, I. Celanović, M. Soljačić, E. N. Wang, *Nat. Nanotechnol.* **2014**, *9*, 126.
[149] A. Vora, J. Gwamuri, N. Pala, A. Kulkarni, J. M. Pearce, D. Ö. Güney, *Sci. Rep.* **2014**, *4*, 4901.
[150] D. Ö. Güney, T. Koschny, C. M. Soukoulis, *Phys. Rev. B* **2009**, *80*, 125129.
[151] H. Deng, T. Wang, J. Gao, X. Yang, *J. Opt.* **2014**, *16*, 035102.
[152] E. W. McFarland, J. Tang, *Nature* **2003**, *421*, 616.
[153] J. Li, S. K. Cushing, P. Zheng, F. Meng, D. Chu, N. Wu, *Nat. Commun.* **2013**, *4*, 2651.
[154] W. Li, J. Valentine, *Nano Lett.* **2014**, *14*, 3510.
[155] a) S. Song, Q. Chen, L. Jin, F. Sun, *Nanoscale* **2013**, *5*, 9615; b) W. Li, Z. J. Coppens, L. V. Besteiro, W. Wang, A. O. Govorov, J. Valentine, *Nat. Commun.* **2015**, *6*, 8379.

[156] M. W. Knight, H. Sobhani, P. Nordlander, N. J. Halas, *Science* **2011**, *332*, 702.
[157] H. Harutyunyan, A. B. Martinson, D. Rosenmann, L. K. Khorashad, L. V. Besteiro, A. O. Govorov, G. P. Wiederrecht, *Nat. Nanotechnol.* **2015**, *10*, 770.
[158] M. E. Sykes, J. W. Stewart, G. M. Akselrod, X.-T. Kong, Z. Wang, D. J. Gosztola, A. B. Martinson, D. Rosenmann, M. H. Mikkelsen, A. O. Govorov, *Nat. Commun.* **2017**, *8*, 986.
[159] Y. Yu, Z. Ji, S. Zu, B. Du, Y. Kang, Z. Li, Z. Zhou, K. Shi, Z. Fang, *Adv. Funct. Mater.* **2016**, *26*, 6394.
[160] A. Sousa-Castillo, M. Comesaña-Hermo, B. Rodríguez-González, M. S. Pérez-Lorenzo, Z. Wang, X.-T. Kong, A. O. Govorov, M. A. Correa-Duarte, *J. Phys. Chem. C* **2016**, *120*, 11690.
[161] a) A. O. Govorov, H. Zhang, Y. K. Gun'ko, *J. Phys. Chem. C* **2013**, *117*, 16616; b) L. V. Besteiro, A. O. Govorov, *J. Phys. Chem. C* **2016**, *120*, 19329.
[162] G. V. Hartland, L. V. Besteiro, P. Johns, A. O. Govorov, *ACS Energy Lett.* **2017**, *2*, 1641.
[163] X. T. Kong, Z. Wang, A. O. Govorov, *Adv. Opt. Mater.* **2017**, *5*, 1600594.
[164] L. V. Besteiro, X.-T. Kong, Z. Wang, G. Hartland, A. O. Govorov, *ACS Photonics* **2017**, *4*, 2759.
[165] Y. Lu, W. Dong, Z. Chen, A. Pors, Z. Wang, S. I. Bozhevolnyi, *Sci. Rep.* **2016**, *6*, 30650.
[166] a) B. Y. Zheng, Y. Wang, P. Nordlander, N. J. Halas, *Adv. Mater.* **2014**, *26*, 6318; b) F. P. García de Arquer, A. Mihi, G. Konstantatos, *ACS Photonics* **2015**, *2*, 950.
[167] a) Z. Fang, Z. Liu, Y. Wang, P. M. Ajayan, P. Nordlander, N. J. Halas, *Nano Lett.* **2012**, *12*, 3808; b) W. Wang, A. Klots, D. Prasai, Y. Yang, K. I. Bolotin, J. Valentine, *Nano Lett.* **2015**, *15*, 7440; c) J. Fang, D. Wang, C. T. DeVault, T.-F. Chung, Y. P. Chen, A. Boltasseva, V. M. Shalaev, A. V. Kildishev, *Nano Lett.* **2017**, *17*, 57.
[168] L. Wen, Y. Chen, L. Liang, Q. Chen, *ACS Photonics* **2017**.
[169] J. Saavedra, A. Asenjo-Garcia, F. J. García de Abajo, *ACS Photonics* **2016**, *3*, 1637.
[170] M. W. Knight, Y. Wang, A. S. Urban, A. Sobhani, B. Y. Zheng, P. Nordlander, N. J. Halas, *Nano Lett.* **2013**, *13*, 1687.
[171] K. Du, Q. Li, W. Zhang, Y. Yang, M. Qiu, *IEEE Photonics J.* **2015**, *7*, 1.
[172] J. Grant, I. Escorcia-Carranza, C. Li, I. J. McCrindle, J. Gough, D. R. Cumming, *Laser Photonics Rev.* **2013**, *7*, 1043.
[173] W. Ma, D. Jia, Y. Wen, X. Yu, Y. Feng, Y. Zhao, *Opt. Lett.* **2016**, *41*, 2974.
[174] S. Cibella, P. Carelli, M. Castellano, F. Chiarelloa, A. Gaggeroa, E. Giovinea, G. Scalaric, G. Torriolia, R. Leonia, *Proc. SPIE* **2017**, *10103*, 101031M.
[175] F. B. Niesler, J. K. Gansel, S. Fischbach, M. Wegener, *Appl. Phys. Lett.* **2012**, *100*, 203508.
[176] F. Zhang, S. Feng, K. Qiu, Z. Liu, Y. Fan, W. Zhang, Q. Zhao, J. Zhou, *Appl. Phys. Lett.* **2015**, *106*, 091907.
[177] N. J. Hogan, A. S. Urban, C. Ayala-Orozco, A. Pimpinelli, P. Nordlander, N. J. Halas, *Nano Lett.* **2014**, *14*, 4640.
[178] D. Chicherin, S. Dudorov, D. Lioubtchenko, V. Ovchinnikov, S. Tretyakov, A. V. Räisänen, *Microwave Opt. Technol. Lett.* **2006**, *48*, 2570.
[179] W. Zhu, A. Liu, T. Bourouina, D. Tsai, J. Teng, X. Zhang, G. Lo, D. Kwong, N. Zheludev, *Nat. Commun.* **2012**, *3*, 1274.